Mitigation of Wide Angle Signal Interference in Terahertz Imaging Systems

by

Mahmoud Shoukry Ahmed Mohamed Sakr

A Thesis Presented in Partial Fulfillment
of the Requirements for the Degree
Master of Science

Approved April 2018 by the
Graduate Supervisory Committee:

Georgios Trichopoulos, Chair
Constantine Balanis
James Aberle

ARIZONA STATE UNIVERSITY

May 2018

ABSTRACT

The objective of this work is to design a low-profile compact Terahertz (THz) imaging system that can be installed in portable devices, unmanned aerial vehicles (UAVs), or CubeSats. Taking advantage of the rotational motion of these platforms, one can use linear antennas, such as leaky-wave antennas or linear phased arrays, to achieve fast image acquisition using simple RF front-end topologies. The proposed system relies on a novel image reconstructing technique that uses the principles of computerized tomography (Fourier-slice theorem). It can be implemented using a rotating antenna that produces a highly astigmatic fan-beam. In this work, the imaging system is composed of a linear phased antenna array with a highly directive beam pattern in the *E*-plane allowing for high spatial resolution imaging. However, the pattern is almost omnidirectional in the *H*-plane and extends beyond the required field-of-view (FOV). This is a major drawback as the scattered signals from any interferer outside the FOV will still be received by the imaging aperture and cause distortion in the reconstructed image. Also, fan beams exhibit significant distortion (curvature) when tilted at large angles, thus introducing errors in the final image due to its failure to achieve the assumed reconstructing algorithm.

Therefore, a new design is proposed to alleviate these disadvantages. A 14×64 elements non-uniform array with an optimal flat-top pattern is designed with an iterative process using linear perturbation of a close starting pattern until the desired pattern is acquired. The principal advantage of this design is that it restricts the radiated/received power into the required FOV. As a result, a significant enhancement in the quality of images is achieved especially in the mitigation of the effect of any interferer outside the FOV. In this report, these two designs are presented and compared in terms of their imaging efficiency along with a series of numerical results verifying the proof of concept.

TABLE OF CONTENTS

CHAPTER Page

LIST OF TABLES

LIST OF FIGURES

Figure Page

Figure Page

Figure Page

Figure Page

Figure Page

CHAPTER 1

INTRODUCTION

1.1 History of Imaging

The history of imaging started as early as humans began observation. People started observing and investigating the optical phenomenon that surrounds them such as reflection, refraction and even the ability of some crystals to magnify images. After many experiments, peoples' knowledge on optics, manufacturing, and packaging grew enough that they were able to make the first practical optical instrument – namely spectacles – in 1270 in Florence, Italy [1]. One step further was achieved by performing image magnification using lenses, thus achieving the first image projection system in the 16th century, known as the magic lantern. Using an oil lamp and a lens, this system could project an image painted on glass plates onto a screen. A figure of one of the oldest known preserved magic lanterns is depicted in Fig 1.1. Afterwards, optical imaging experienced further improvements including the invention of the compound microscope as a two-element optical system, the development of artificial glass fabrication, the derivation of geometrical optics laws especially the refraction law, and many other milestones that allowed the development of modern imaging techniques.

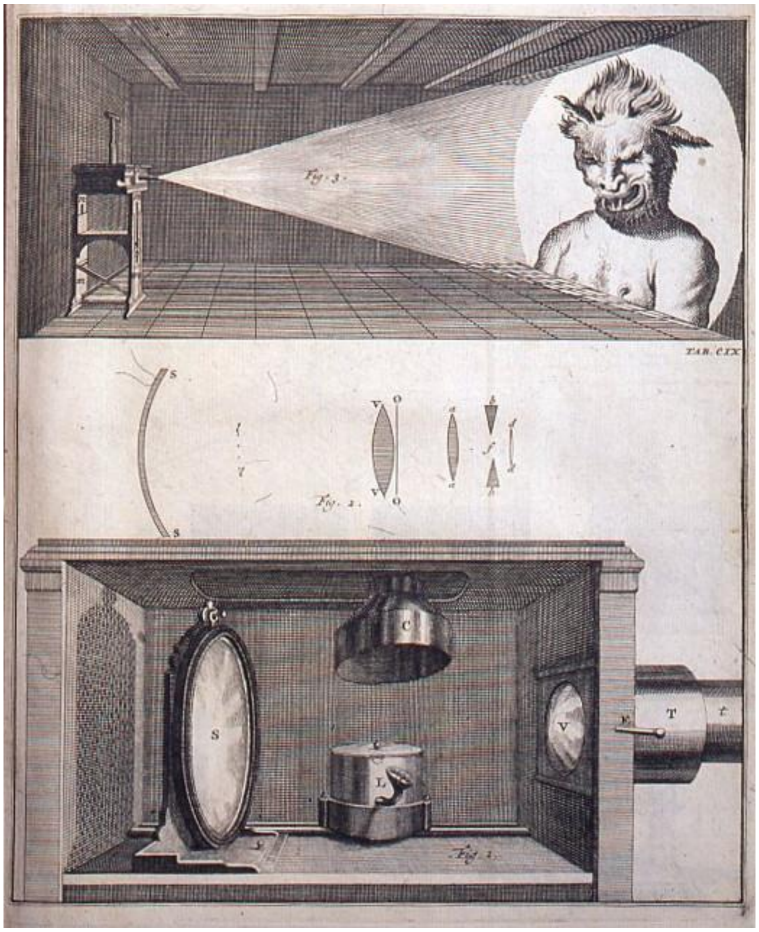

Figure 1-1 One of the oldest preserved magic lanterns projecting a monster (Source: A page of Willem's Gravesande's 1720 book Physices Elementa Mathematica).

However, some drawbacks of the properties of visible waves prevent it from being used in certain imaging applications. As most of the materials are opaque to light waves, researchers are not able to use visible light in medical imaging, for example, when the goal is to see underneath the skin and inside organs. Similar problems are encountered in remote sensing, that is, to be capable of observing earth's subsurface. As such, there is a need for radiation capable of penetrating through materials that are opaque in the visible electromagnetic spectrum. For instance, medical imaging has gone through a lot of remarkable achievements since the discovery of x-rays [2], [3]. With its special penetrating characteristics through the body's tissues, x-rays represented a revolutionary method to perform medical imaging. More advancements have been achieved later in this field with innovative technologies, such as magnetic resonance imaging (MRI), ultrasound, and computed tomography (CT). These new technologies have also given rise to the importance of image reconstruction algorithms. Often, collected data cannot directly be interpreted into meaningful images, and proper post-processing is required to reconstruct the geometry of the field of view (FOV).

Lately, the science and engineering communities have started investigating the capabilities of the last unexploited part of the electromagnetic spectrum. Terahertz (THz) radiation (300 GHz – 10 THz) features unique electromagnetic properties, and the developments of semiconductor technology and nanofabrication techniques have produced devices with cutoff frequencies exceeding 1 THz [4]. Having the advantage of small wavelength, THz radiation can penetrate through materials opaque to other parts of the EM spectrum. Packaging materials; including paper, cardboard, textiles, plastics, wood, ceramics, semiconductors, and dried and frozen materials are semi-transparent. Despite the great interest in this technique since the 1920s [5], the THz spectrum remained unexplored for a long time due to lack of powerful sources and sensitive detectors. This intermediate frequency gap between the microwave region and the optical range, as shown in Fig 1.2, experiences high propagation losses that reduced the commercial emphasis on THz systems. Moreover, the lack of the available instrumentation at these high frequencies was another obstacle. Having signal generators and detectors, measurement devices, etc. at such frequencies was very challenging for a long time. It was not until 1960 when the first image was generated using the THz radiation [6]. Again, it took researchers till 1995 to achieve another significant advancement in this field when the THz time-domain spectroscopy was used to generate the first THz image [7] that sparked the improvement of THz imaging technology.

Two THz-images were presented in this publication are shown in Fig 1.3. In Fig 1.3 (a), a transmitted THz signal integrated over 1-3 THz frequency range was used to construct the image of a silicon chip inside its packaging. The figure shows only a little absorption in the THz spectral range from the plastic packaging, while the silicon chip and the metal connectors are clear. This image consists of 50,000 pixels with a roughly 250 μm spatial resolution. Another image was generated and shown in Fig 1.3 (b) that detects the water distribution within a leaf. The figure shows a THz image for the leaf when it was freshly cut (Left) and another THz image of the same leaf after 48 hours (Right). Although the leaf visibly looks almost the same with no significant change during that time span, the THz image shows an appreciable change in the water content of the leaf. Both images consist of 30,000 pixels with a spatial resolution of 400 μm.

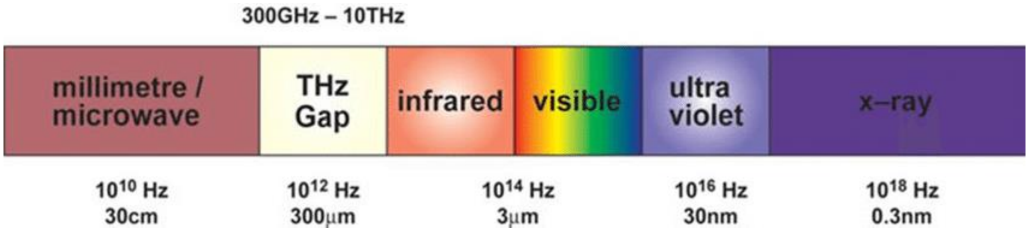

Figure 1-2 The THz gap among the electromagnetic spectrum (Source: A G Davies et al., “The Development of Terahertz Sources and their Applications,” Physics in Medicine and Biology, Oct 17, 2002).

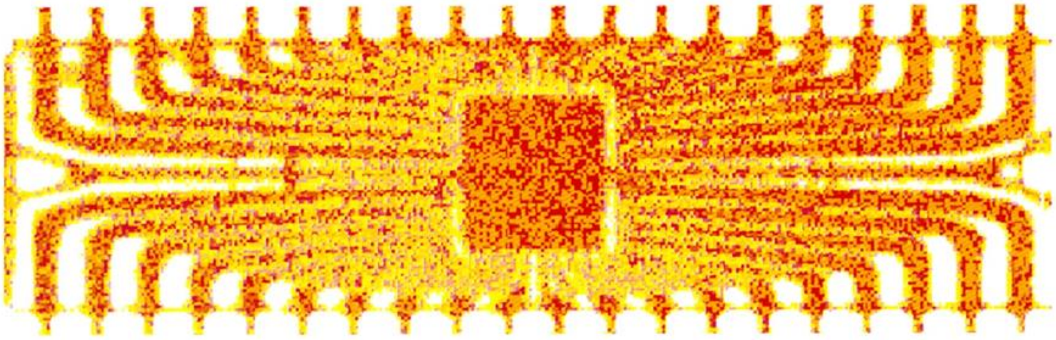

Plate I. THz image of a packaged semiconductor integrated circuit (plastic packaging).

(a)

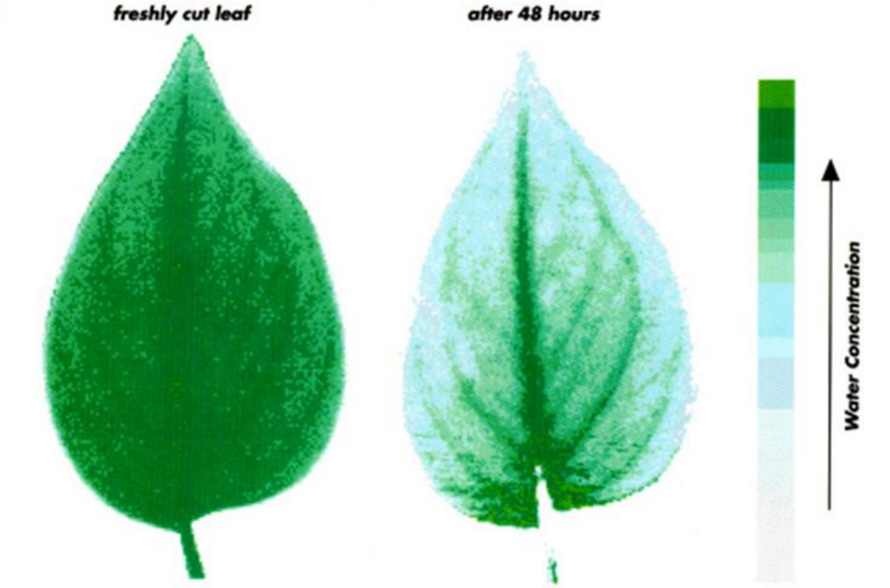

Plate II. Left: THz image of a fresh leaf. Attenuation of THz radiation through the leaf is largely due to water within the leaf. Right: THz image of the same leaf after 48 h. Water has clearly evaporated from the leaf, except from the stems of the leaf. At the far right is the color scale indicating the relative water concentration within the leaf; darker green corresponds to higher water concentration.

(b)

Figure 1-3 The first reported THz images generated by THz time-domain spectroscopy, (a) THz image of a silicon chip inside its plastic packaging, and (b) two THz images of the same leaf showing the change in its water content after 48 hours from being cut (source: B. B. Hu et al., "Imaging with terahertz waves," Opt. Lett. 20, 1716-1718 (1995)).

1.2 Applications of THz Imaging

Millimeter Wave (mmWave) and Terahertz (THz) wave applications have attracted the attention of the research community due to their small wavelengths that enable the design of high spatial resolution radar imaging systems. As such, imaging systems at these frequencies can be utilized for applications in non-destructive inspection, security, surveillance, and earth and space observation [9]-[31]. Additionally, the short wavelength can lead to a compact imaging system that could be embedded in lightweight unmanned aerial vehicles (UAVs) or CubeSats that demand lightweight/low-profile devices.

1.2.1 Properties of THz Radiation

THz radiation has a lot of distinct advantages over other regions of the spectrum. First, a wide range of optically opaque materials is transparent at THz frequencies allowing the waves to penetrate and reveal details behind these materials. Secondly, this part of the spectrum has low energy photons and accordingly it is non-ionizing radiation, thus, safe for biological tissues. Moreover, images captured by THz systems can have high spatial resolutions because of the small wavelengths of the THz spectrum. For instance, a resolution of 150 nm THz imaging was reported in 2003 using near-field probing [32]. These short wavelengths also allow for some essential measurements in difficult-to-probe materials. Several materials have unique absorption spectral patterns at THz frequencies allowing for the usage of THz radiation in the identification of these materials [11]- [14]. Some of these applications are explained in more detail in this section.

1.2.2 Astronomy and Space Observation Applications

Due to its high penetrability and spatial resolution, THz systems are very important for space observation. In space astronomy, THz radiation can be utilized to provide answers to questions about the formation of stars and how galaxies were initially formed [24], [25]. As the radiation at the THz spectrum has high penetrability, it was proven that THz radiation could be used to examine the cores of the dark clouds to reveal the dust from which new stars and planets are formed. For environment monitoring, a THz imaging system can be used to monitor the depletion mechanisms of the ozone layer as there is a large number of atmospheric molecules such as water, nitrogen, oxygen, and carbon monoxide that can be detected in the THz band [26].

1.2.3 Surveillance and Security Applications

THz imaging is very efficient in spectroscopy and material identification [11]-[14]. The absorption of electromagnetic radiation that ranges between 0.1 and 4 THz produces a unique spectral pattern that can identify several materials. These absorption fingerprints can be used in security applications to detect explosives from a distance as they continually emit trace amounts of vapor [30]. For instance, by transmitting a THz pulse through the suspicious material, a strong absorption will occur at certain frequencies that represents a fingerprint for each different material. Fig 1.4 shows the fingerprints of explosives and explains how they are distinguishable from clothing or other inert materials that could cover them. Moreover, fabrics and plastics are semi-transparent to this range of frequencies, so it can also be used for security screening to detect concealed weapons or other suspicious objects. For example, Fig 1.5 shows a THz image of a dummy explosives belt hidden beneath the clothes.

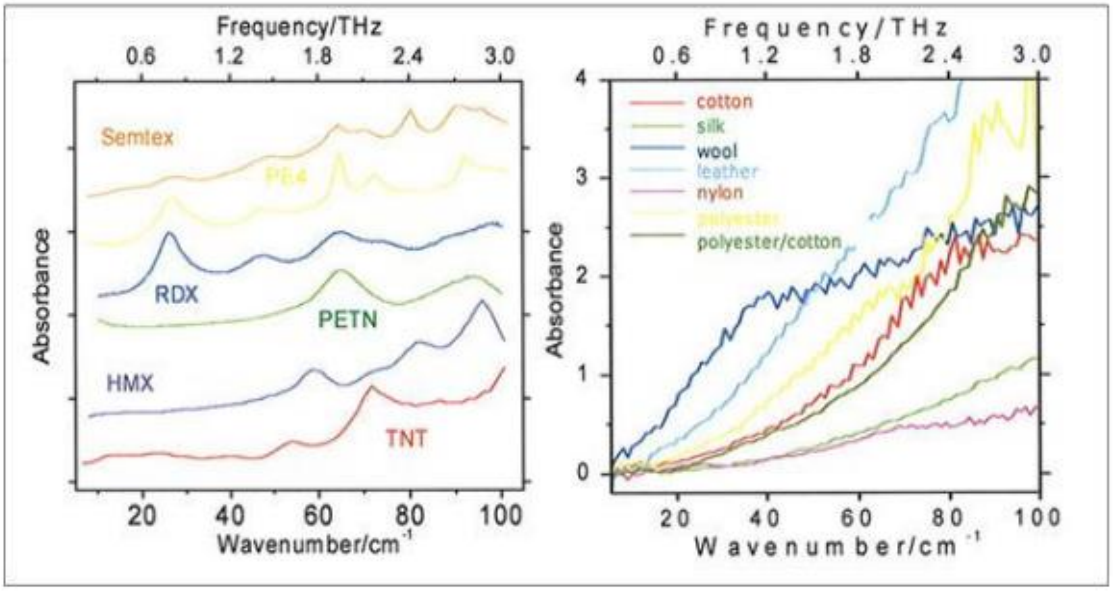

Figure 1-4 THz fingerprints of explosives and clothing materials (Source: Ergün, S., Sönmez, S. (2015). Terahertz Technology for Military Applications, Journal of Military and Information Science, Vol3(1),13-16).

Figure 1-5 A THz image of a dummy explosives belt (Courtesy of TeraSense Development Labs).

1.2.4 Biomedical Applications

THz imaging can also be applied in medical imaging applications. Unlike conventional X-rays, THz radiation is non-ionizing, which means that its low photon energies do not damage the tissues and DNA [8], [21]. It can also detect differences in water content and density of tissue [27]- [29]. Such a method can be used to identify cancer tumors with safe, painless imaging systems.

1.2.5 Quality Control and Non-destructive Testing

This technique can be considered as a non-destructive evaluation technique [22], [23], that is a technique to evaluate the properties of a material, especially for dielectrics, without causing damage. It can play a significant role in the inspection of multilayer structures and can identify abnormalities or defects. For example, Fig 1.6 shows a THz image of a chocolate bar that contains a stone, a glass splinter, and a metal screw. Experiments showed that these undesirable contaminants are distinguishable from the possible ingredients like raisins and nuts.

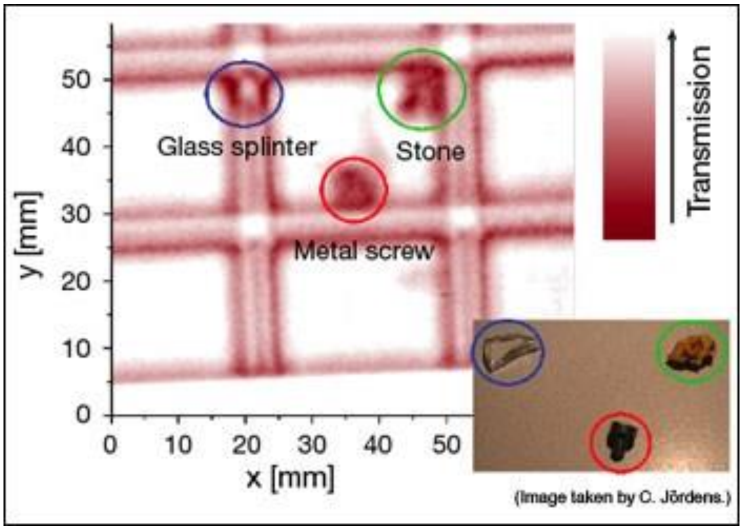

Figure 1-6 A THz image of a chocolate bar that distinguish undesirable contaminants from the original ingredients (Source: OPN Issue March 2007, page 21).

1.2.6 Military Applications

THz waves-based radars have a lot of advantages that conventional radars do not have for military applications. As most stealth techniques are based on narrow-band coating surfaces, the wideband radiation of a THz pulse would enable the radars to detect these structures, allowing them to possess an anti-stealth technology [30], [31]. In [30], military trailers and stealth tank models are imaged and detected using a THz radar. Fig 1.7 shows a T72 tank scale model and its reconstructed image by a THz radar at 1.56 THz. Also, in [31] a study of the THz radar cross section (RCS) of scale models of airplanes is presented for F16 and F35 fighters. As shown in Fig 1.8, a scale model of the F16 aircraft is reconstructed using THz imaging. The letter marks indicate positions of different scattering parts of the airplane model: wing tips (WT), wing (W), tail (T), fuselage (F) and missiles (M1, M2). The figure shows the ability of the THz imaging system to reconstruct major parts of the stealth aircraft.

Also, the detection of landmines represented a big issue for a long time as most of the ground penetrating radar systems cannot distinguish these small mines from rocks. However, using THz spectroscopic imaging, the detection of landmines is possible as non-metallic objects hidden beneath soil can be detected. A proof of concept was done for a non-metallic landmine [30].

Nevertheless, the usability of such systems for most of the afore-mentioned applications depends mainly on the high integrability and cost of the system. Therefore, reducing the total number of the radiating elements in the final system, while performing high-resolution imaging, is crucial for such applications. The following part briefly illustrates the previous work done in this domain and the scope of this study.

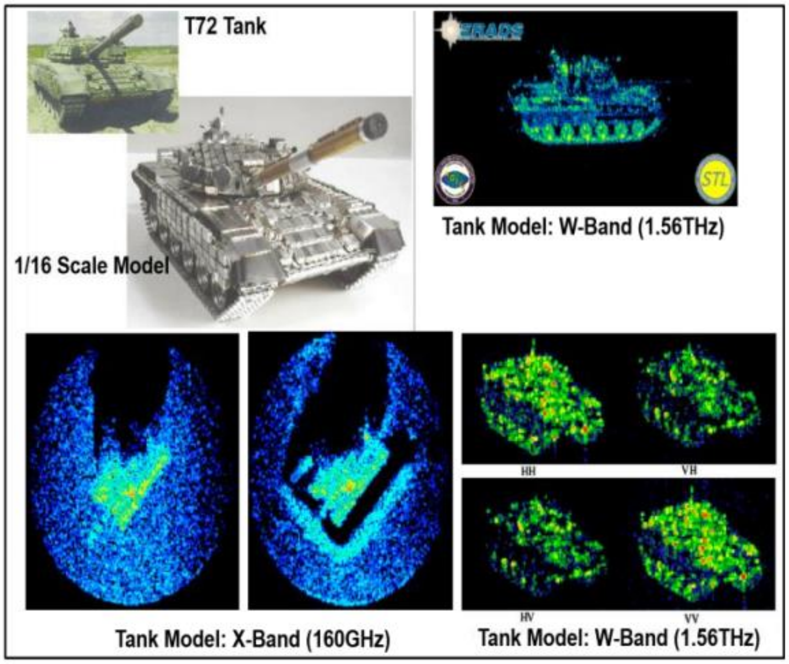

Figure 1-7 A THz image of a T72 Tank model (source: Ergün, S., Sönmez, S. (2015). Terahertz Technology for Military Applications, Journal of Military and Information Science, Vol3(1),13-16).

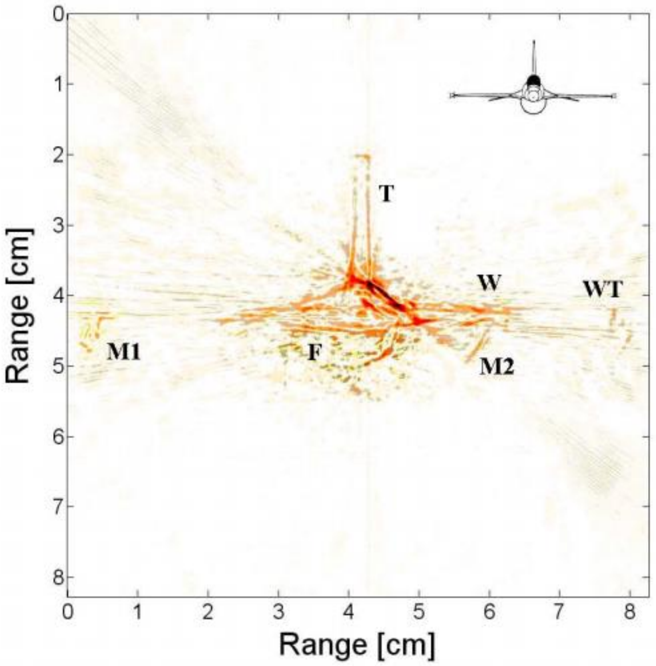

Figure 1-8 A THz reconstructed image of scale model of the F16 fighter (Source: Iwaszczuk, K., Jepsen, P. U., & Heiselberg, H. (2012). Terahertz Technology for

Defense and Security-Related Applications. Kgs. Lyngby: Technical University of Denmark (DTU)).

1.3 A Literature Review and the Scope of this Study

In general, THz imaging systems perform high-resolution imaging exploiting either quasi-optical setups [12], antenna arrays [13]- [17] or a combination of both [18], [19]. However, acquiring high spatial resolution images demands for large aperture sensors leading to extremely bulky topologies. Moreover, since the spacing between sensors in the antenna array is proportional to the wavelength, which is very small at these frequencies, THz systems suffer from a high density of radiating elements, and accordingly, high RF front-end complexity. To compensate for these obstacles, raster scanning, or other synthetic aperture imaging techniques have also been implemented leading to simplified RF front-ends [15]- [18]. Nevertheless, for large-scale imaging systems that generate high-resolution images, complexity remains high and they exhibit slow image acquisition speed, therefore; their proliferation is limited.

A robust technique to reduce the imaging sensor complexity is the application of multistatic sparsity techniques [16]- [18]. For example, Ahmed *et al.* in [16] proposed a multistatic imaging system that performs imaging at 78 GHz and the field-of-view (FOV) is 160×160 cm at a 50 cm distance from the sensor. This system relies on a raster scanning technique that inherently requires using a large number of elements to produce a highly directive pencil beam. However, this number of elements is reduced significantly by sparsely populating the sensor's aperture using 768 receiving and 768 transmitting elements. Although the effective number of elements used is 768^2, the total number of channels/elements is 1,536 leading to a bulky and complicated design, as shown in Fig 1.9. In [17], Baccouche *et al.* proposed a W-Band multistatic imaging system comprised of two linear arrays (12 receiving and 12 transmitting horn antennas). However, this system acquires images by performing a synthetic aperture technique, where linear scanning is necessary to synthesize the THz image, dramatically limiting image acquisition speed. Alternately, Nowok *et al.* [18] proposed a multiple input multiple output (MIMO) 3D imaging system at 360 GHz, implemented by two linear arrays. The FOV is scanned by beam steering, which is partially achieved by mechanically manipulating a quasi-optical system, resulting in a bulky design. Therefore, even though using multistatic sparsity techniques reduces the total number of elements, the existing solutions remain bulky and complex.

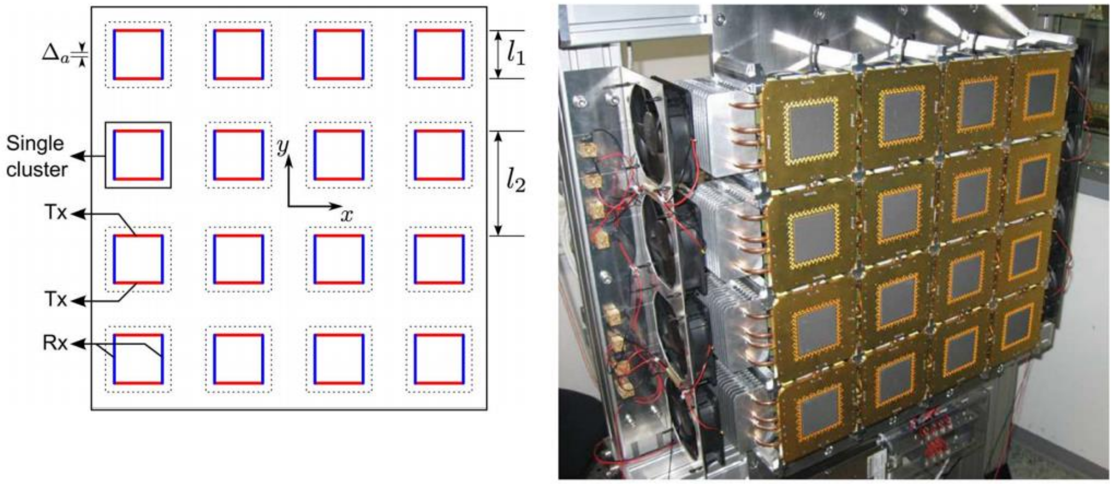

(a) (b)

Figure 1-9 The proposed design by Ahmed et al. that significantly decreases the number of required elements from 768^2 to only 1,536 using sparsity technique (a) the multistatic sparse array geometry, and (b) the front side of the implementation of the imager.

The scope of this work is to design a low-profile system that performs high-resolution radar imaging while retaining a low-profile and a simplified-compact RF front-end. The recent advances in integrated circuits for mmW/THz applications [33]-[35], along with sparsity techniques [36] and existing image reconstruction algorithms [37], [38], can be exploited to design a low-profile, compact imaging system, like the one proposed herein. This system can be used either in security, surveillance, or earth observation applications. Namely, it can be installed in portable devices, UAVs or CubeSats, where high integration is dire.

The proposed system is comprised of a rotating phased array (Fig. 1.10) that operates as a monostatic or a multistatic imaging radar and performs high-resolution 2D or 3D images. Imaging is performed by mechanically rotating the antenna array around its center, while electronically scanning the fan-beam. Then, the image is synthesized by applying the same technique used in the computerized tomography, called Fourier-slice theorem [38]. As such, the novel imaging approach allows for a low-profile, lightweight, and cost-effective topology that can be attractive for several mmW and THz imaging applications. As depicted in Fig. 1.10, the proposed sensor can utilize the capability of certain UAVs to rotate (yaw axis) and provide rapid image acquisition.

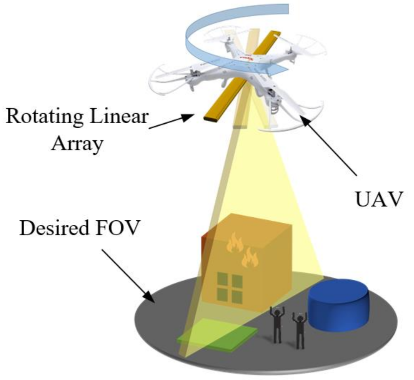

Figure 1-10 An Application example of the proposed imaging system comprised of a rotating linear phased array.

1.4 Outline of the Thesis

This thesis is organized as follows. Chapter 2 discusses the Fourier-slice theorem, a technique to reconstruct images using the backscattered data of an object when illuminated by highly directive fan beams. In Chapter 3, indicative antenna designs that can be used to generate a fan beam to scan the required FOV are presented including the design of a flat-top beam array that is optimized for this imaging technique with highlights on its design procedures. The simulation of the imaging problem is computationally intensive and a recently introduced modeling technique is used to simplify this problem, as presented in Chapter 4, along with the simulation results of imaging of some simple targets and comparisons between the efficiency of the proposed antenna designs. A final summary, conclusions, and future work are detailed in Chapter 5.

CHAPTER 2

IMPLEMENTING THE FOURIER-SLICE THEOREM IN 2D THz IMAGING

One of the main pillars of imaging is the processing of the collected data from the target to reconstruct its image. In this work, the imaging system relies on the same image reconstructing technique used in the computerized tomography (CT), namely, the Fourier-slice theorem. This chapter discusses computerized tomography, the theory of image reconstruction, and finally, presents a discussion about the ability of this technique to simplify the system in terms of weight, size, and cost.

2.1 Application of Fourier-Slice Theorem in 2D THz Imaging

Tomography is the type of imaging that is performed by illuminating a target from many different directions and collects the reflected or transmitted data to reconstruct a cross-sectional image of a semi-transparent object [38]. This technique was first applied in diagnostic medicine to allow for the safe and precise diagnosis of the internal organs of the patient. Specifically, Computerized Tomography (CT) made use of x-rays because of its ability to penetrate different human tissues with varying attenuation coefficients. Then, the image of the tissue is formed based on its x-ray attenuation coefficient. This image reconstruction process relies on the Fourier-Slice Theorem [38] whose applications are not limited only to medical applications. The same technique is utilized for numerous non-medical applications, such as remote sensing using a spotlight synthetic radars (SARs) [40], which employ the same algorithms used in the CT to reconstruct terrain images based on the scattered wavefronts. Another example is the work presented here, as the idea of the Fourier-slice theorem is being applied in THz imaging to simplify the whole system making it smaller and lighter and allowing for nearly real-time image acquisition.

The basic idea of the Fourier-slice theorem relies on forming the image of the FOV from its projections. The projection of the FOV at a given angle is equivalent to the integral of the FOV in the direction specified by this angle. While the integrations are being measured along straight lines through the object and are referred to as line integrals as shown in Fig 2.1. Each line integral represents the integral of some physical parameter along a line, while this parameter will represent different physical phenomena depending on the imaging problem that is considered. For example, in an x-ray CT, this parameter corresponds to the attenuation of x-rays as they propagate through biological tissue, while in an ultrasound CT this line integral will represent the propagation of a sound wave as it travels through the object.

From a mathematical point of view, the Fourier-slice theorem [38] relates the Fourier transform of the measured projections to the two-dimensional Fourier transform of the object's surface or cross section. Then, there are many reconstruction algorithms derived from this theorem, depending on the type of projection used, which could be a parallel beam projection, a fan beam projection, etc. However, in our case, we are interested in the parallel beam projection type, as illustrated in Fig 2.1. The algorithm that is currently being used in most of the applications is the filtered back-projection (FBP) algorithm [38]. In the next section, the principles of the Fourier-slice theorem and its application in the image reconstruction is presented with a brief explanation of the FBP algorithm.

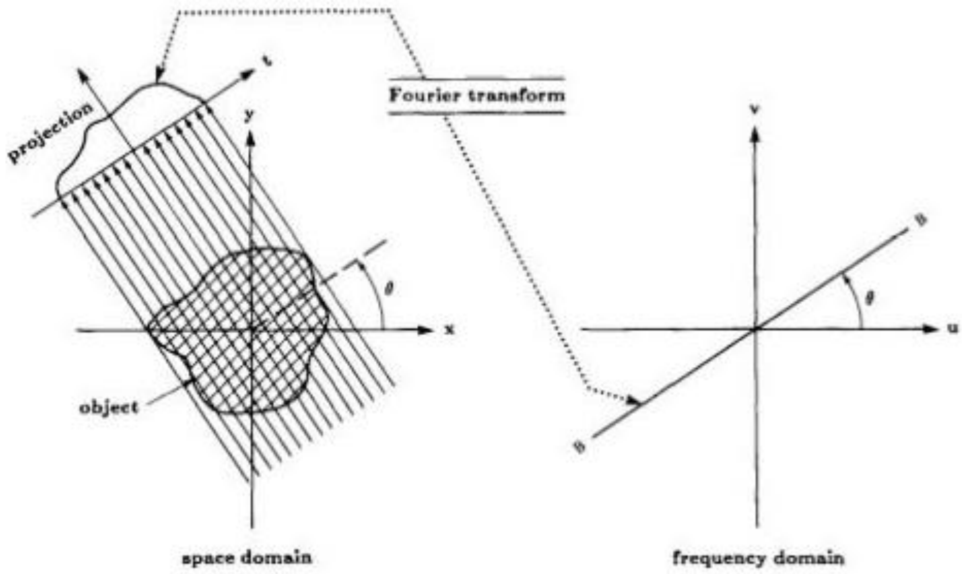

Figure 2-1 The relation between the Fourier transform of a projection at a certain angle and the Fourier transform of the 2D object along a radial line that represents a slice of the two-dimensional Fourier transform of the object (Source: A. C. Kak and M. Slaney, "Principles of Computerized Tomographic Imaging," IEEE Press, 1988).

2.2 Image Reconstruction using the Fourier-Slice Theorem

The first mathematical solution to the problem of reconstructing a function from its projection was first presented by Radon in 1917 [42]. In his paper, Radon proposed that the image of a two-dimensional object, or any cross-section of a three-dimensional object, can be reconstructed from its projections that are obtained by the rotational scanning. The line integral across the beam path, which is also known as the Radon transform, is defined as

$$P_\theta(t) = \int f(x,y)ds \tag{2.1}$$

Where (*ds*) is a differential length on the beam path, the line equation of a ray from the projections is defined by: $t = x\cos\theta + y\sin\theta$, and the function *f(x,y)* in our case represents the reflectivity of the object's surface to the THz beams. While the integration is performed by a set of parallel rays that illuminate the surface of the object and scattered back to be detected by the antenna sensors. A projection $P_\theta(t)$ is a collection of the set of the line integrals formed by all the parallel beams at a fixed rotation angle (θ). The Fourier slice theorem then starts by taking the one-dimensional Fourier transform of this parallel projection at a certain angle which is related to a slice of the two-dimensional Fourier transform of the original object (refer to Fig 2.1). Then, by repeating the same procedure at enough angles, the two-dimensional Fourier transform of the object's surface or cross-section can be estimated, as illustrated in Fig 2.2. Finally, the image can be reconstructed from the projection data at all the rotation angles by simply performing the two-dimensional inverse Fourier transform. The two-dimensional Fourier transform of the object is defined as [38]

$$F(u,v)=\int_{-\infty}^{\infty}\int_{-\infty}^{\infty} f(x,y)e^{-j2\pi(ux+vy)}dxdy \tag{2.2}$$

And the Fourier transform of the projection data $P_\theta(t)$ at a certain angle θ, is [38]

$$S_\theta(\omega)=\int_{-\infty}^{\infty} P_\theta(t)e^{-j2\pi\omega t}dt\ \forall\theta \tag{2.3}$$

where (ω) is the spatial frequency. As the radiation source rotates to different angles, the coordinate system also should be rotated, so the previous result could be generalized in terms of a (t,s) coordinate system representing a rotated version of the original (x,y) system, where

$$\begin{bmatrix} t \\ s \end{bmatrix} = Q_\theta \begin{bmatrix} x \\ y \end{bmatrix} = \begin{bmatrix} \cos\theta & \sin\theta \\ -\sin\theta & \cos\theta \end{bmatrix} \begin{bmatrix} x \\ y \end{bmatrix} \tag{2.4}$$

and (Q_θ) is the rotation matrix between the circular and cartesian coordinate system. Note that the rotation is performed from 0 to π since the additional information is redundant. After acquiring all the necessary projections, the Inverse Radon Transform (IRT) is used to reconstruct the final image [38]

$$f(x,y) = \int_0^{\pi} Q_\theta \left[\int_{-\infty}^{\infty} S_\theta(w) |w| e^{j2\pi wt} dw \right] d\theta \tag{2.5}$$

However, in practice, the system can only measure a finite number of projections, and therefore, the Fourier transform of the object will only be known at a limited number of radial lines as shown in Fig 2.2. This fact will bring up the need to interpolate from these data to continue all the required data to perform the inverse Fourier transform. And as a result of dealing with polar coordinates, the sampling rate, or the density of the measured points, is decreasing as we go further away from the center which increases the interpolation error also. That's why the direct usage of the Fourier transform in practical applications is not common. Instead, the filtered back projection algorithm [38] is used in order to add a specific weight to each measured projection to correct for any image degradation possible as a result of this interpolation error.

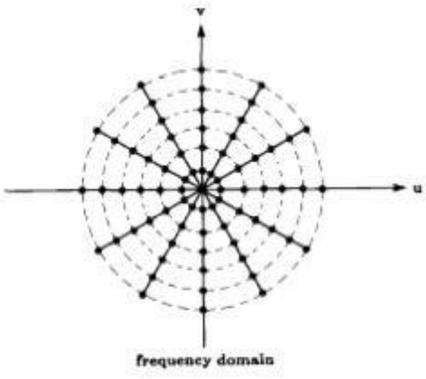

Figure 2-2 After a set of projections are taken for the object at different angles, a collection of Fourier transforms of the object at different radial lines can be estimated with an accuracy that depends on the density of the radial points (Source: A. C. Kak and M. Slaney, "Principles of Computerized Tomographic Imaging," IEEE Press, 1988)

This mathematical transformation algorithm is implemented in the imaging system as illustrated in Fig 2.3. The imaging scheme comprises an antenna array that produces an electronically-controlled beam that illuminates only a linear portion of the field of view (FOV) and measures the backscattered signal. The controlled beam is then electronically swept across the object area, scanning it strip-by-strip as shown in Fig 2.3. The recorded signals of every beam sweep correspond to a single projection of the Radon transform. Then, this phased array is rotated azimuthally ($0\text{-}180^o$) repeating the parallel beam scanning in multiple discrete azimuth angles. Namely, for each rotation angle θ, a single Radon projection is obtained. This set of projections is called the RT of the target. The calculated RT should meet certain sampling criteria. To reconstruct a correctly sampled image, the number of parallel rays ($N_{parallel}$) should be approximately equal to the number of rotational projections ($N_{projections}$) [38]. Finally, the object's image is reconstructed using the inverse Radon transform of the collected data.

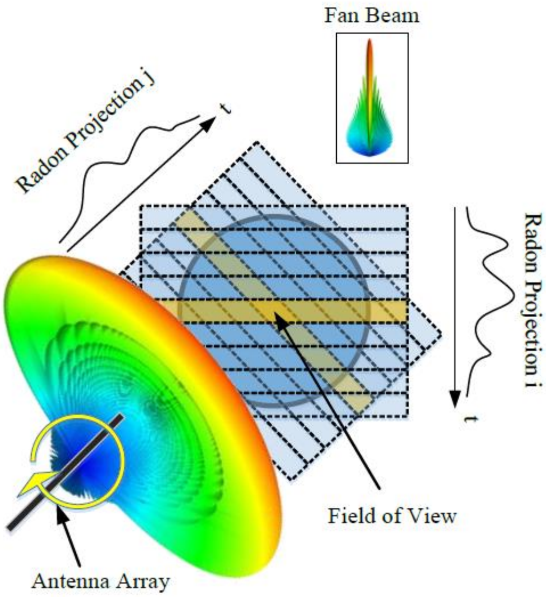

Figure 2-3 The implementation of the Fourier-slice theorem using a phased-antenna array that illuminates and scans the FOV strip-by-strip and repeats the scanning at different projection angles from 0° to 180° (Source: P. C. Theofanopoulos et al., "A novel THz radar imaging system using the radon transform," 2017 IEEE APS National Radio Science Meeting, San Diego, CA, 2017, pp. 1513-1514).

However, the rotating nature of this imaging technique has an inherent drawback that should be noticed and taken into account. As shown in Fig 2.3, the antenna at each position has a rectangular FOV determined by its beamwidth in one dimension and the number of strips it scans in the other dimension. Let's assume that both sides are equal and will represent this width by (L) as shown in Fig 2.4. As the antenna rotates to a different position to perform a new projection, this rectangular FOV is rotating respectively to include different parts of the object scene that were not captured by the previous antenna position FOV. As the antenna rotates from 0° to 180°, a total circular FOV is being formed with a diameter of (√2 * L). The portion of the object that is sufficiently sampled, is the common area seen by all observation angles of the rotation antenna array. This condition is satisfied only in the inner circle shown in Fig 2.4, with a diameter equal to (L) which represents the correctly imaged part of the FOV. However, all the points in the ring between the inner and outer circles will be undersampled, and the reconstructed image of any object in this region will be distorted. Apparently, any point farther away from the outer circle is not sampled at all and any object there, ideally, will not be imaged. So, in reality, the antenna design should take into consideration that its radiation pattern is restricted only inside the desired FOV. If the radiation of the antenna extends beyond it, it might illuminate interferers outside the FOV causing distortion to the image of the required target.

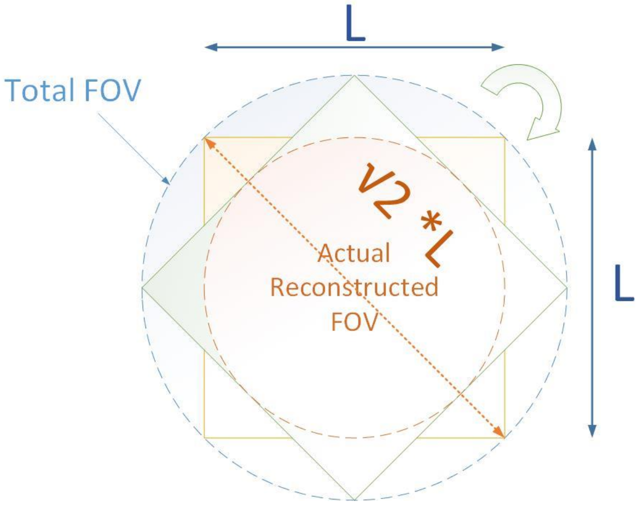

Figure 2-4 An illustration of the actual reconstructed FOV as a result of rotating the antenna and the FOV respectively.

As an illustrative example to the previous process, a spherical target at 15° from the z-axis in the FOV of a linear uniform array with fan beam radiation, as depicted in Fig 2.5, is to be imaged. The array scans the FOV line by line and records the projections, then it is rotated, and the scanning is repeated. The projections are shown in Fig 2.6 at rotation angles of 30°, 60°, 90°, 120°, 150° for both x- and y-polarizations of the source's radiation (the used simulation algorithm is illustrated in detail in chapter 4). These projections can be organized in a sinogram as the one shown in Fig 2.7 (a). A sinogram shows the variation of the magnitude of the projection at each projection angle with the scanning of the FOV.

For instance, in this case, when the array is at its initial position (0°) the max coupling happens at almost 15° which is the location of the target. Also, the magnitude of the maximum coupling is increasing and reaches its maximum when the projection angle is almost 15° at which the maximum gain of the radiation pattern is in the direction of the target. Then, as the array rotates, the location of the maximum coupling shifts towards a smaller scanning angle as the relative position of the target with respect to the array is changing. Also, the magnitude of the maximum coupling is decreasing as the direction of the maximum gain of the array is more and more tilted away from the target until the array is rotated by almost 90° from the target's location. After that, the maximum coupling starts to increase again, until the array reaches 180° rotation at which the array will see the target at -15°. Finally, the inverse Radon transform is applied and the image of the FOV is reconstructed in Fig 2.7 (b).

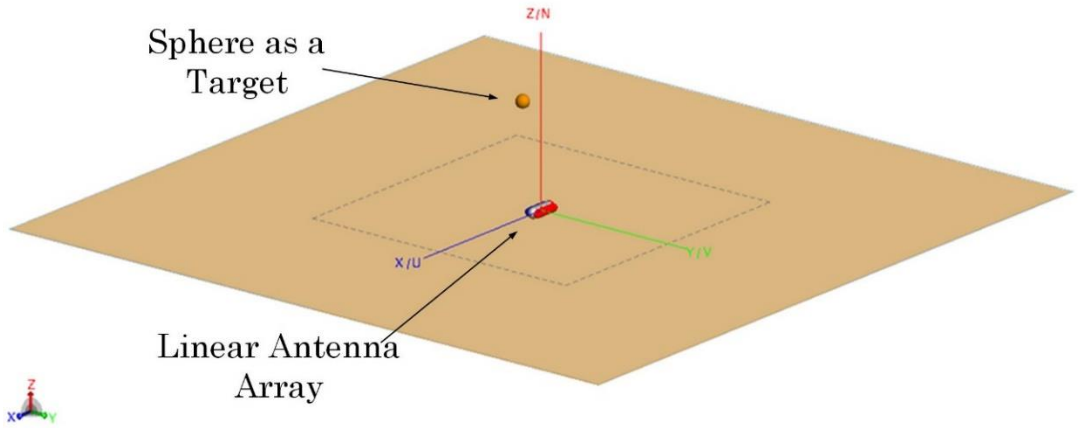

Figure 2-5 A conventional setup to simulate the imaging process of a target using the Fourier-slice theorem technique

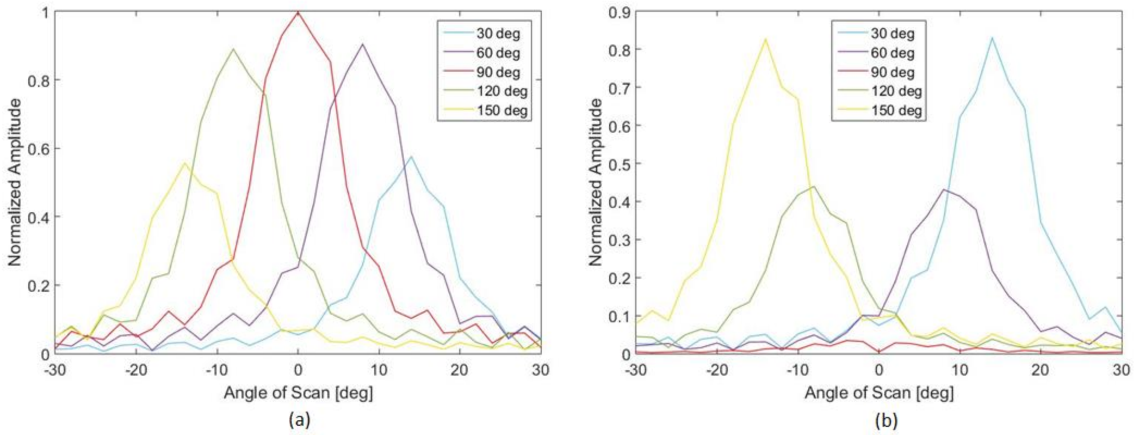

Figure 2-6 The projections of the FOV at different projection angles for the (a) x-polarization, and (b) y-polarization of the source's radiation.

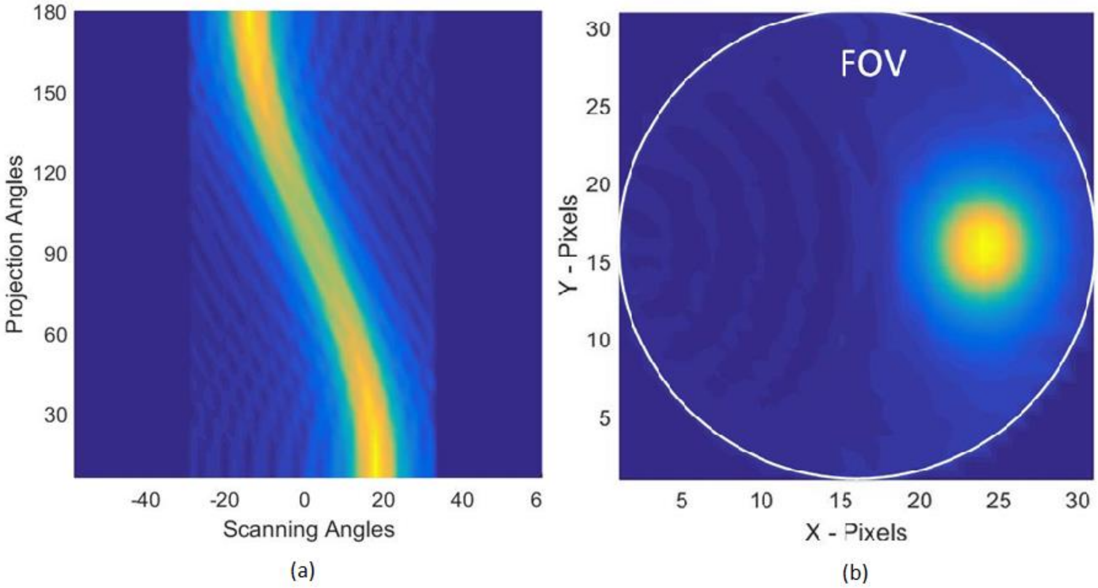

Figure 2-7 (a) The sinogram of the projections shown in Fig 2.6, and (b) the reconstructed image of the FOV.

2.3 Advantages of using the Fourier-Slice Theorem Imaging Technique

One of the major challenges in mmWave and THz imaging is the need for a large number of radiating elements to achieve high-resolution imaging, and therefore more complicated transceivers are required. For the system to be able to acquire information on both the amplitude and phase of the scattered signals, mixers and local oscillators (LOs) should be used, with the need also for the LOs routed and synchronized through the system. All these issues will have a direct impact on the complexity of the feeding network, the power consumption, total size, weight, and cost of the system.

However, using the Fourier-slice theorem allows overcoming these drawbacks as it allows to reconstruct the image with illuminating only a linear portion of the FOV at a time instead of illuminating a pixel-by-pixel as in the pencil-beam scanning technique. Therefore, a wider beamwidth radiation pattern is required to illuminate the total width of the FOV at a time, instead of illuminating a single pixel. This fact allows for a significant reduction in the number of elements of the array, and accordingly, the required transceivers leading to a much simpler RF front-end and a more compact system.

In the next chapter, the discussion is extended to the different antenna designs and beamforming techniques that could be used along with the Fourier-slice theorem to perform imaging. A comprehensive comparison between these techniques is presented. Afterwards, two phased array designs are presented and compared in terms of their number of elements, radiation patterns, and their imaging efficiency. A comparison with the pencil-beam scanning case is also presented.

CHAPTER 3

ANTENNA DESIGNS FOR IMAGING USING THE FOURIER-SLICE THEOREM

In this chapter, the design of antennas that can implement the Fourier-slice theorem in imaging is presented. These antennas are required to electronically scan the FOV line by line at different projection angles and collect the data to reconstruct the image of the FOV. In general, to achieve this purpose, the required antenna needs to have a fan-beam type of radiation patterns to illuminate a linear portion of the FOV at a time. Also, this antenna has to be able to sweep this beam electronically to scan the whole FOV such as the leaky-wave antennas (LWA) and phased-array antennas. Two phased-array designs with fan-beam patterns are presented in detail and compared regarding their imaging efficiency after a brief overview about the leaky-wave antennas. Also, a discussion about the feeding network of such antennas and some techniques to simplify these complex networks is presented.

3.1 Fan-Beam Generation by Leaky-Wave Antennas

One source of a fan-beam radiation pattern is leaky-wave antennas. The leaky-wave antenna is a member of the traveling-wave antennas family that is recognized by having almost uniform voltage distribution along them, in contrast with the standing wave or resonant antennas [43]. This is achieved by properly terminating the antenna, so the reflections are minimized. A simple explanation of the idea of the leaky-wave antennas is that it radiates small increments of power, either continuously like a dielectric slab that radiates as the wave is traveling inside it, or discretely like a slotted rectangular metallic waveguide as the one shown in Fig 3.1. The traveling fields inside the structure decay along the direction of wave travel and increase in others. The one-dimensional leaky-wave antenna exhibits a fan beam radiation pattern. This beam is scanned by changing the frequency of the traveling wave inside the structure, that is, the electrical distance between the slots of the waveguide is changing as the frequency changes leading to direct the maximum radiation in different directions.

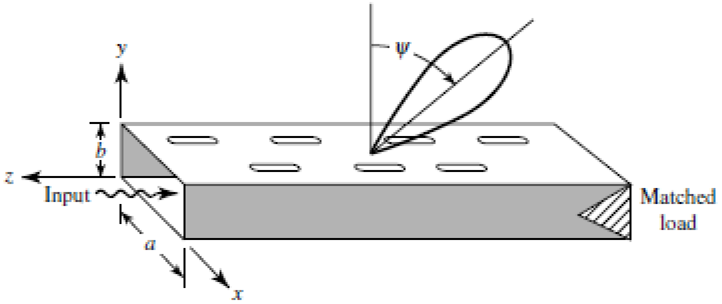

(a) Upper wall—longitudinal

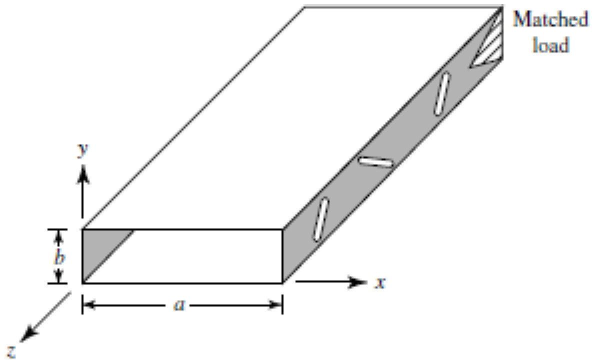

(b) Sidewall—inclined

Figure 3-1 A general schematic of a leaky wave antenna showing the decaying of the propagated fields as waves are traveling inside it (Source: C. A. Balanis, Antenna Theory: Analysis and Design. John Wiley & Sons, 2016).

The major advantage of leaky-wave antennas is that it needs only one source to excite the antenna. And by changing the frequency of this source, the radiated beam is tilted to the desired direction. While for the phased-array antennas, a complex feeding network is essential as complex transceivers are required, as discussed earlier in chapter 2. Thus, a significant reduction in the system complexity can be achieved by using leaky-wave antennas. However, the leaky-wave antenna needs to use some frequency span to scan the beam between the required angular limits. Thus, any information related to a frequency in this span cannot be extracted. For instance, changing the frequency in the phased antenna arrays could be used to generate information about the depth of the target instead of only reconstructing an image for its surface. Also, for material exploration applications, the whole object is required to be scanned at the same frequency so any frequency-related information, e.g. resonance, can be revealed which is not the case when each part of the object is scanned at a specific different frequency.

3.2 Fourier-Slice Theorem Implementation using Phased Antenna Arrays

Another source of fan-beam radiation patterns is the uniform linear phased-antenna arrays. Like the leaky-wave antennas, the uniform phased-arrays have their own advantages and disadvantages. While, one of the main advantages for using phased-array antennas over leaky-wave antennas is that it can sweep its beam at a single frequency while maintaining the frequency information to be used depending on the application. In this section, two phased-array antenna designs are presented with a detailed discussion about the design approach of each of them and a comparison between their efficiency in imaging and, also, with the case of pencil-beam scanning phased array.

3.2.1 A Uniform Linear Phased Array

The usage of antenna arrays is essential in most of the practical designs to synthesize any desired radiation pattern, as any single antenna element exhibits a specific radiation pattern that can't be changed. However, utilizing multielement antenna allows for controlling the shape of the radiation pattern by choosing the suitable excitations and geometrical arrangement of these elements.

For instance, an essential advantage for the implementation of the Fourier-slice theorem is the ability to sweep the beam of the antenna to perform electronic scanning for the FOV. This beam sweeping can be achieved in antenna arrays by controlling the relative shift in the excitation phase of the successive elements. Also, in order to achieve higher spatial resolutions, the generated fan beam needs to be very directive having a small half-power beamwidth (HPBW), which is one of the advantages gained by using multielement antenna.

The proposed design consists of a uniform, equally spaced N-elements, linear array of half-wavelength dipoles with equal excitation amplitudes for all the elements. The array factor (AF) of such an array can be designed, assuming no coupling between the elements of the array, using [43]

$$AF = \sum_{n=1}^{N} e^{j(n-1)(kd\cos\theta+\beta)} = \sum_{n=1}^{N} e^{j(n-1)\psi} \tag{3.1}$$

where (N) is the number of elements in the array, (d) is the spacing between the elements, (θ) represents the observation angle, and (β) is the difference in the phase excitation between each two successive elements. By choosing a certain spacing between the elements, the direction of the maximum radiation can be controlled by adjusting the progressive phase shift between the elements (ß) so that [43]

$$For\ \psi = kd\cos\theta + \beta|_{\theta=\theta_0} = kd\cos\theta_0 + \beta = 0 \tag{3.2}$$

$$\beta = -kd\cos\theta_0 \tag{3.3}$$

where (θ_0) is the angle of the maximum radiation. As such, the accompanied feeding network should be able to continuously change the progressive phase shift (β) between the elements, which increases the complexity of the whole system as we increase the number of elements.

For this specific design, the spacing is chosen to be half wavelength ($d=\lambda/2$), where the elements are placed above at the height of a quarter wavelength ($h=\lambda/4$) above a ground layer. The array sweeps the main radiation lobe within the $-90° \leq \theta_0 \leq 90°$ range, depending on the width of the required FOV to be imaged. It is clear from (3.1) that as (N) increases, the gain will increase to allow for higher spatial resolution imaging. A comparison between the radiation patterns of 16, 32 and 64 elements cases, all simulated at a frequency of 300 GHz, are shown in Fig 3.2. Also, the HPBW and gain of each of them are presented in table 1. From the comparison, it is seen that as the number of elements is increased, the HPBW in the *E*-plane of the pattern decreases and the gain increases leading to a narrower and a more directive fan beam.

Table 1

A comparison between the HPBW and the gain of a 16-element, 32-element, and 64-element uniform linear arrays.

	16-element Linear Array	32-element Linear Array	64-element Linear Array
HPBW (E-plane)	6.14°	3.09°	1.46°
HPBW (H-plane)	120°	120°	120°
Gain [dBi]	17.06	19.99	22.97

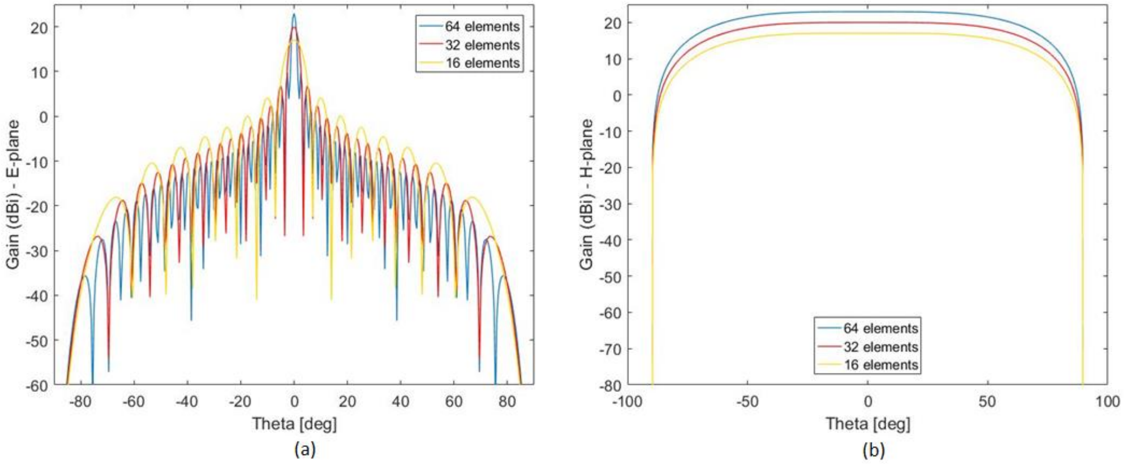

(a) (b)

Figure 3-2 A comparison between the radiation patterns of a 16-element, 32-element, and 64-element linear uniform arrays: (a) The *E*-plane, (b) The *H*-plane.

As the beamwidth of the fan beam decreases, the angular resolution of the resulting images increases allowing the imaging system to distinguish between closer details in the FOV. A testing case shown in Fig 3.3 is performed to compare the angular resolution of the 16-element and 64-element uniform linear arrays. This testing case comprises four plane waves representing targets at angular locations of 8°, 10°, 14°, and 20° where both the 16-elements and 64-elements linear arrays in comparison are trying to image them and distinguish between all these four targets. The resulting images using both antennas are depicted in Fig 3.4. The 16-elements case shows that the antenna is not able to distinguish between any of these targets and the resulting image is as if there is one big target in this region. However, using the 64-elements array, the image shows four distinct targets as the real situation.

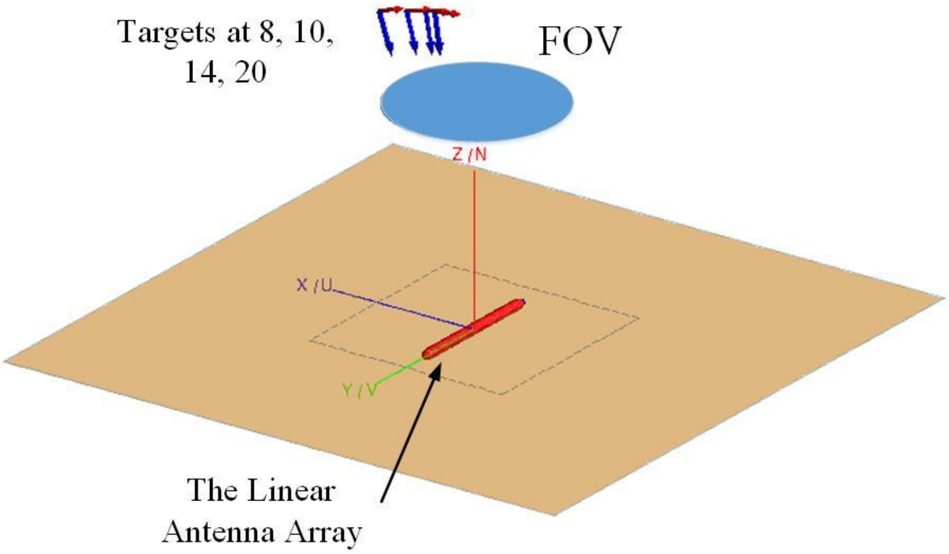

Figure 3-3 The angular resolution testing setup showing four plane waves representing targets at angular spacings of 2°, 4°, and 6°.

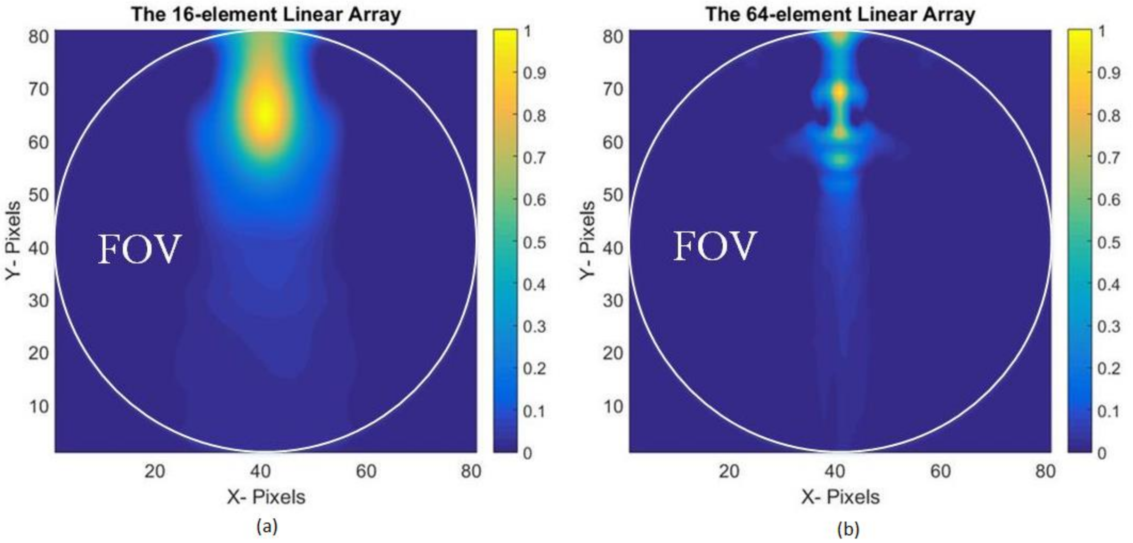

Figure 3-4 The resulting images using (a) the 16-elements, and (b) the 64-elements linear arrays.

As a result, the 64-elements array design was chosen with the elements placed horizontally in a collinear arrangement to decrease the mutual coupling between the dipoles as the radiation pattern of a dipole obtains nulls at both of its ends. The physical structure of the array is illustrated in Fig 3.5 with a three-dimensional view of its radiation pattern showing the directive fan beam at a scanning angle of $\theta_0 = 0°$.

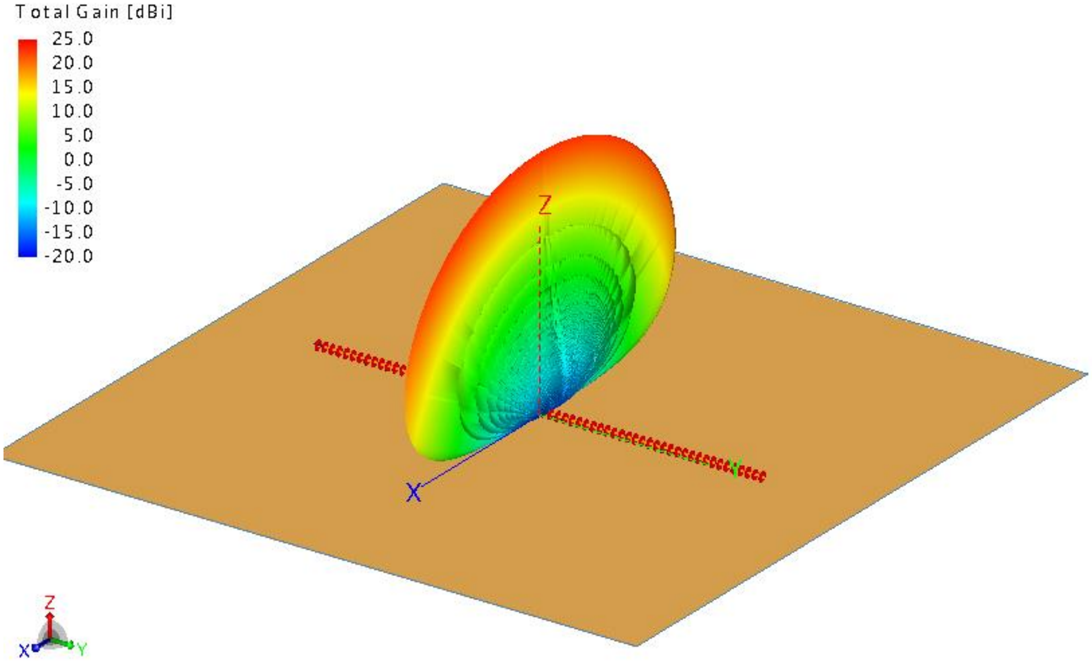

Figure 3-5 A 64-element uniform linear array at a height of $\lambda/4$ above a perfect PEC plane showing the 3D radiation pattern of the array at an angle $\theta_0 = 0°$.

In the imaging process, the fan beam is scanned from a starting angle (θ_1) to another angle (θ_2), thus defining the size of the FOV along the beam sweep direction. The size of the FOV on the perpendicular direction is determined by the fan beam HPBW on the *H*-plane, which is seen from Fig 3.2(b) and table 1 to be very wide (around 120°) and almost omnidirectional regardless the number of elements used in the array. Referring to Fig 3.6, the actual FOV illuminated by this array is extended beyond the desired FOV. As a result, the scattered signal from illuminated objects outside the FOV can cause interference in the received signals from targets in the desired FOV and distort the synthesized radar image. So, although having the advantages of being simple and compact, and having an almost uniform gain in the desired FOV, this design suffers from the wide beamwidth in the *H*-plane with no control on it with the available design parameters, which represents a major limitation on the imaging efficiency of this design. For instance, if the required FOV dimensions are 40°×40°, the beam will be scanned from -20° to 20° in the *E*-plane. However, the other dimension is not controlled, and it will be as wide as the HPBW of this beam in the *H*-plane. One solution for this issue is to synthesize a flat-top beam pattern with a limited HPBW that is determined upon the desired FOV dimensions. As such, by reducing the gain of the antenna in the *H*-plane and forming a flat-top beam, a significant reduction in interference can be achieved resulting in a direct enhancement in the radar image quality.

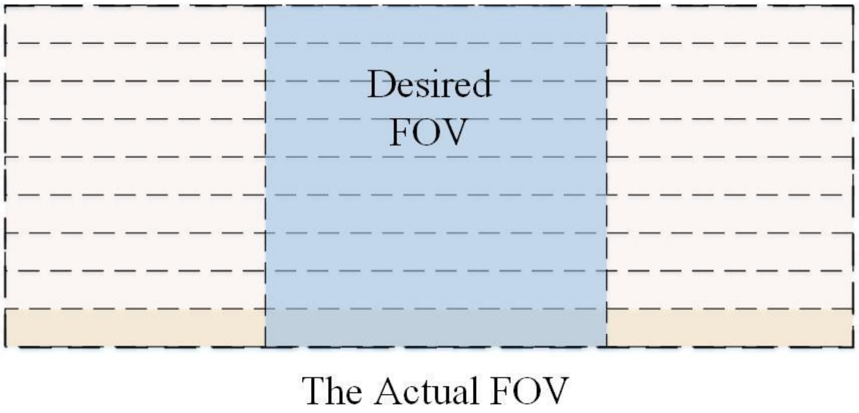

Figure 3-6 A comparison between the actual and desired FOV (at a certain projection angle) of the uniform linear array design showing the possible interference that might happen in case of having any interferers outside the desired FOV.

Another disadvantage in this design results from the curvature of the generated beam, especially with tilting at higher angles as shown in Fig 3.7. This curved pattern revokes the assumption of making a parallel beam projection imaging, the technique that is used in the post-processing steps, which is adding some error to the reconstructed image.

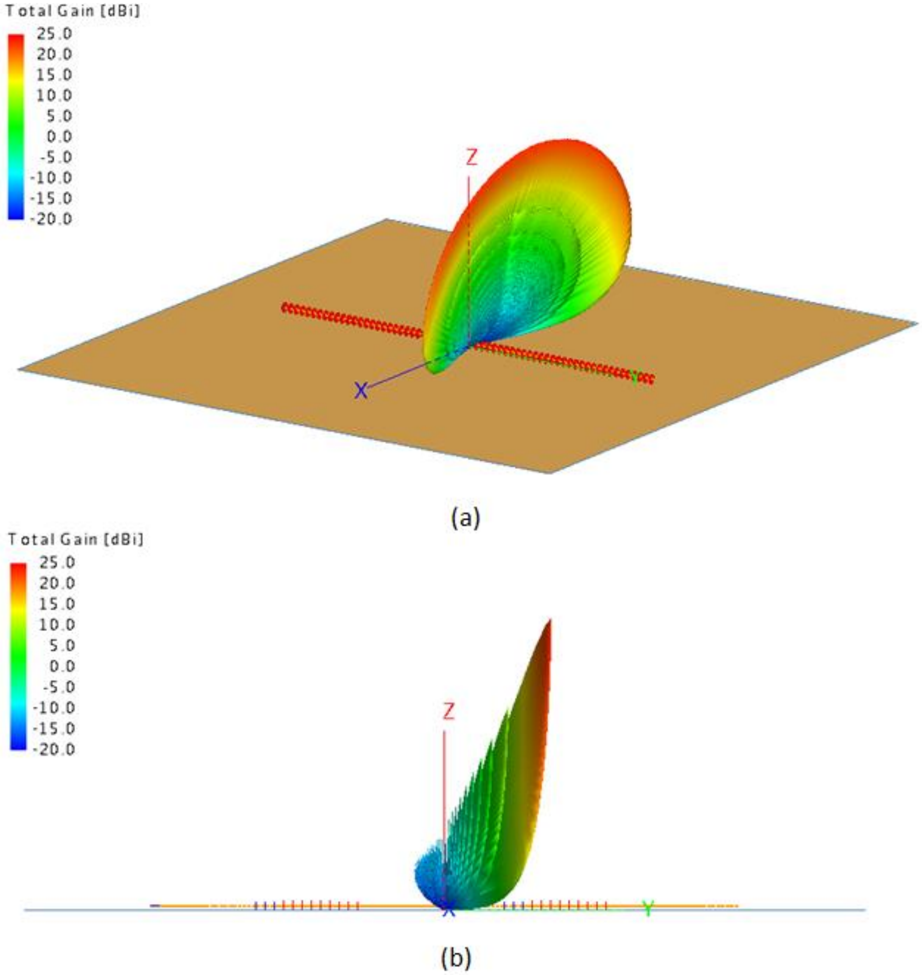

Figure 3-7 The 3D radiation pattern of the 64-element uniform linear array at a scanning angle of $\theta_0 = 20°$ showing the curvature of the beam from (a) the isometric view, (b) a side view.

Alternately, a novel flat-top beam antenna array was designed to limit the radiation within a specified FOV. The HPBW of this beam in the *H*-plane can be controlled during the design process depending on the required FOV dimensions leading to a suppressed reception of signals from outside this FOV.

3.2.2 A Flat-Top Schelkunoff-Synthesized Phased Array

To mitigate the interference effect from possible interferers, the antenna has to avoid transmitting or receiving signals to/from outside the FOV. Therefore, the objective of this design is to generate a fan beam radiation pattern that can be tilted to scan the FOV, but with additional features of being able to limit its beamwidth into the required FOV dimensions and having almost a constant gain over this FOV. Being flat-top beam radiation, this beam can scan all the parts of the target inside the FOV uniformly, namely, with the same power illuminating each point on the surface of the target. The process of designing an antenna starting from a pre-specified radiation pattern to find the suitable antenna configuration, geometrical dimensions, and the excitation coefficients is called synthesis [43]. There are a lot of synthesis methods reported in the literature; the suitable method should be chosen depending on the required pattern. In this work, an optimization algorithm that utilizes linear perturbations on an initial pattern until achieving the desired pattern is used. This starting pattern is synthesized using the Schelkunoff synthesis method [44] as will be discussed.

3.2.2.1 The Schelkunoff Synthesis Method

This method is usually used when the pattern is required to have nulls in certain directions [44]. Based on the number of nulls and their directions, the number of elements in the array and their excitation coefficients can be derived. Since the array factor (AF) of a non-uniform, equally spaced N-elements arrays is given as [43]

$$AF = \sum_{n=1}^{N} a_n e^{j(n-1)(kd\cos\theta+\beta)} = \sum_{n=1}^{N} a_n e^{j(n-1)\psi} \tag{3.4}$$

where (a_n) represents the excitation coefficient of each element as we are dealing with a non-uniform array and it could be a complex number. This AF function can be represented as a polynomial function in terms of the complex variable inside the summation, say (z). Defining [43]

$$z = x + jy = e^{j\psi} = e^{j(kd\cos\theta+\beta)} \tag{3.5}$$

Then, (3.4) can be rewritten as [43]

$$AF = \sum_{n=1}^{N} a_n z^{n-1} = a_1 + a_2 z + a_3 z^2 + \cdots + a_N z^{N-1} \tag{3.6}$$

which is a polynomial of degree (N-1), that could be expressed as the product of its (N-1) roots as [43]

$$AF = a_n(z - z_1)(z - z_2)(z - z_3)\ldots(z - z_{N-1}) \tag{3.7}$$

where z_1, z_2, z_3, …, z_{N-1} are the roots of the polynomial. And as (z) is a complex number with a magnitude of unity, its value can always be represented on a unit circle, usually referred to as Schelkunoff's circle, while the phase of (z) is dependent on the values of d, θ, β. So, for a specific array with a certain spacing (d) and a progressive phase shift (β), the value of (z) will correspond to a physical observation angle (θ). As shown in Fig 3.8, (z) will have a region of realizable values, in which (θ) ranges between 0 to π, which may or may not cover all the possible values on the unit circle, depending on the values of (d) and (β). The region of the realized values of (z) usually called the Visible Region (VR), while the rest of the values are called the Invisible Region (IR). For Instance, Fig 3.8 shows four different cases in which (β) = 0 but with different values for the spacing (d), we can see that all the possible values of (z) lies in the (VR) only when d = λ/2.

It's clear also from (3.7) that for a certain (z) in the (VR) that corresponds to a specific observation angle (θ), the magnitude of the (AF) depends on the product of the distances between (z) and all the roots from z_1 to z_{N-1} and the phase depends on the summation of phases between (z) and the roots also. So, when a certain root lies on the VR of the unit circle, it will represent a null in the (AF) of this array. This null will occur at the observation angle (θ) that corresponds to the location of this root, as the distance between (z) and this root in (3.7) will vanish.

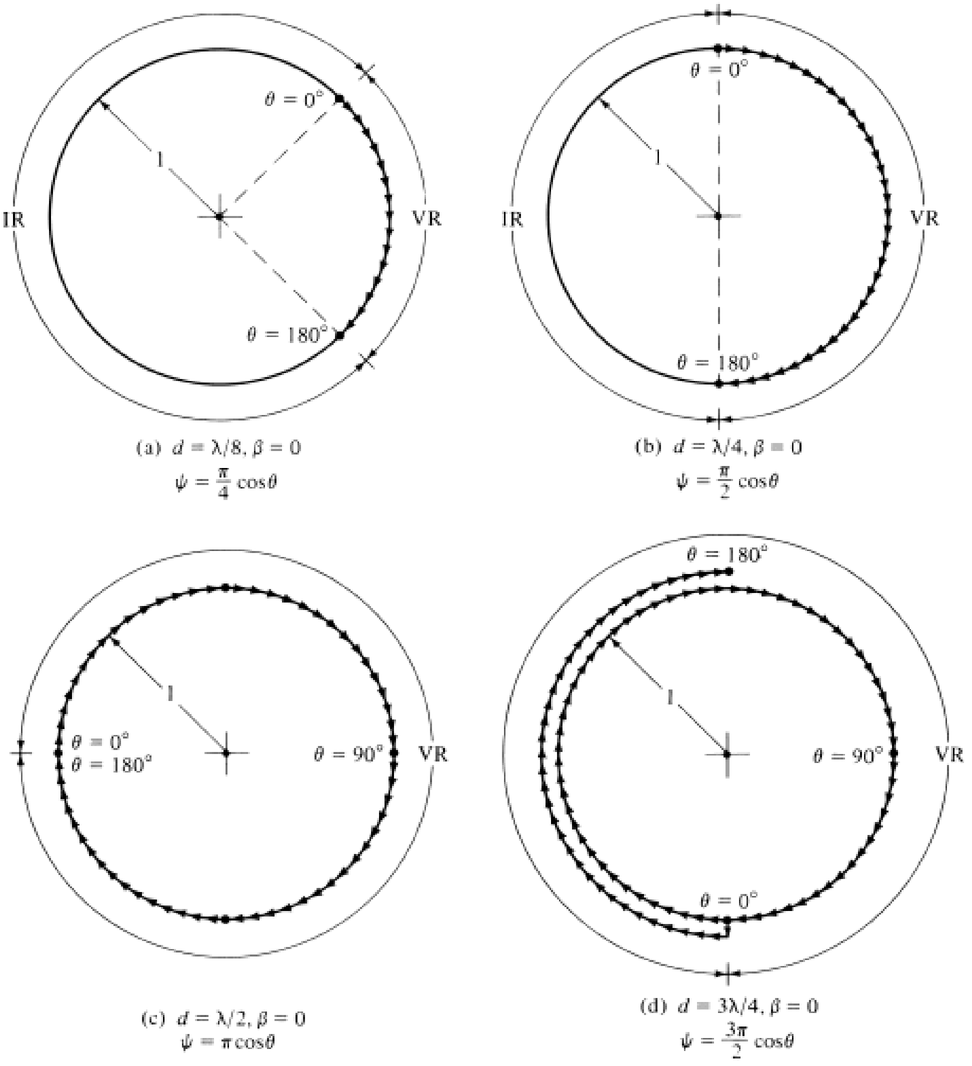

(a) $d = \lambda/8, \beta = 0$
$\psi = \frac{\pi}{4}\cos\theta$

(b) $d = \lambda/4, \beta = 0$
$\psi = \frac{\pi}{2}\cos\theta$

(c) $d = \lambda/2, \beta = 0$
$\psi = \pi\cos\theta$

(d) $d = 3\lambda/4, \beta = 0$
$\psi = \frac{3\pi}{2}\cos\theta$

Figure 3-8 Different cases for the VR of the AF on the unit circle, where (β) = 0 for all cases but for different spacing (d) (Source: C. A. Balanis, Antenna Theory: Analysis and Design. John Wiley & Sons, 2016).

It is very important at this step to notice that any root that does not lie on the (VR) will not contribute to the nulls of the AF, either this root is on the unit circle in the (IR), or it is inside or outside the unit circle. This is illustrated geometrically in Fig 3.9 where only roots (z_4) and (z_7) contribute to the nulls of this AF, while (z_6) is in the (IR) and the others are either inside or outside the unit circle. All of this information is very useful for the design of the (AF) of the array knowing the number of the required nulls and their desired directions.

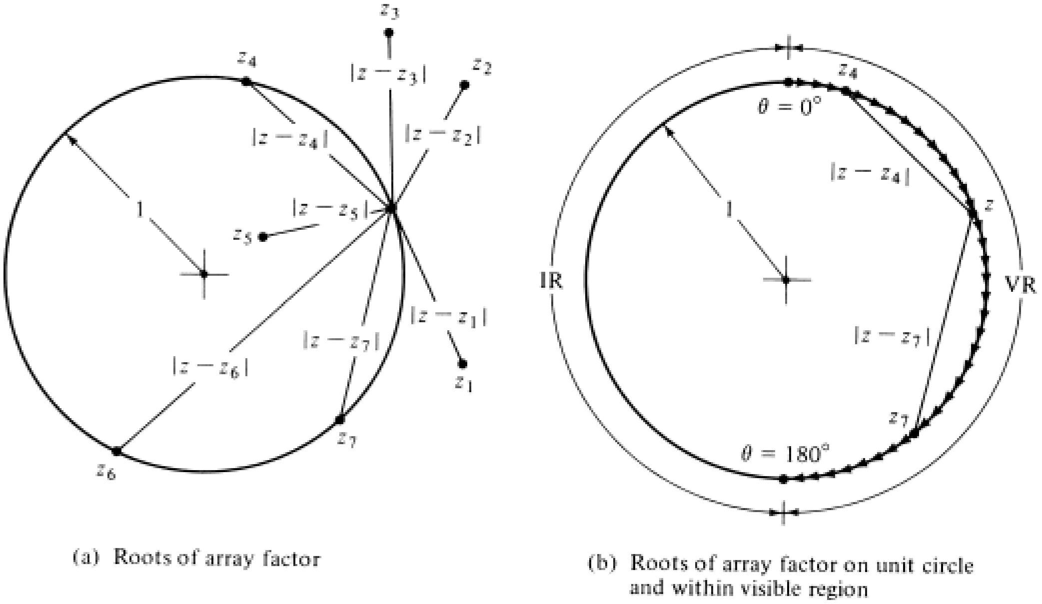

(a) Roots of array factor

(b) Roots of array factor on unit circle and within visible region

Figure 3-9 (a) An example of an AF that has 7 roots distributed inside and outside the unit circle, (b) only those roots on the circle in the VR accounts for the AF nulls (Source: C. A. Balanis, Antenna Theory: Analysis and Design. John Wiley & Sons, 2016).

3.2.2.2 The Design Approach and Radiation Pattern

A novel technique to synthesize the radiation pattern of the array with any required shape, with the ability also to control the side lobe levels was presented by Elliott in 1982 [45]. This technique is based on an iterative optimization technique starting from an initial pattern until the required specifications are achieved. Such a technique is very advantageous in a plethora of applications that needs enough control on the shape of the main beam as well as the side lobes. For instance, high directive beams are required in radars with low side lobes which can’t be easily achieved as the decrease of the sidelobe level comes at the cost of decreasing the directivity also. One solution for this tradeoff is to tolerate high side lobe levels in directions that will not affect the performance of the radar. This will lead to the need for uneven side lobe topology that can't be achieved without a powerful tool to control the beam shape and its side lobes. In the imaging applications, a flat-top beam with symmetric side lobes at the lowest possible level, ideally no sidelobes as the mask shown in Fig 3.10, is required to focus all the power in the FOV uniformly without any extensions outside it.

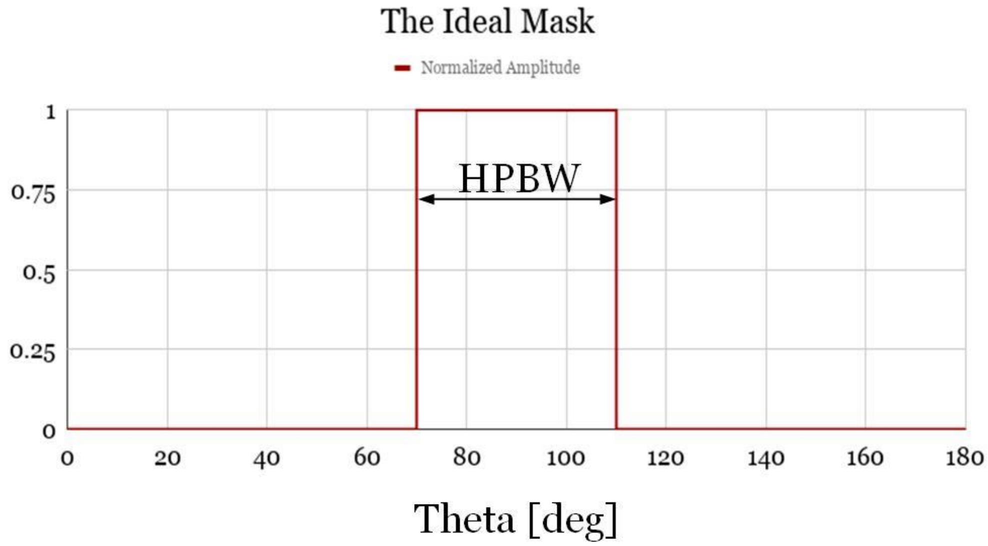

Figure 3-10 The ideal mask of the required flat-top beam to be synthesized.

The first contribution to solving such a problem was presented by Dolph in 1946 [46] to synthesize a sum pattern. In his paper, Dolph found the root positions on the Schelkunoff unit circle that correspond to the excitation coefficients that will produce the Chebyshev pattern, which consists of a main narrow beam with all the side lobes at the same height. The same result was then achieved by Taylor [47] for continuous sources instead of using a discrete array of elements, the result that is then extended by Bayliss [48] for the case of difference patterns. So, using continuous sources, one could start from Taylor or Bayliss patterns and achieve any desired pattern using a linear perturbation technique. This resulting current distribution can also be sampled to derive the excitation coefficients in the case of a discrete array. However, the conventional sampling methods may not be accurate enough, so a perturbation method should be applied until the exact excitation coefficients that will produce the required pattern are achieved. However, as the perturbation will be applied anyway at some certain step, one could start from a known discrete excitation, like the Dolph-Chebyshev, and use the perturbation method to get the required excitation coefficients for the desired pattern. A major disadvantage of this method is that if the chosen starting pattern is not very close to the desired one, the convergence time will be too high as a high number of iterations will be required.

However, the technique presented by Elliot overcomes this disadvantage by linearly perturbing the root locations on the Schelkunoff unit circle. This technique is proved to converge rapidly to the desired pattern even if the starting pattern was poor. For the ease of presentation, the design steps are summarized, and the interested reader is referred to [45] for more details about the technique and the utilized equations.

This synthesis process starts by defining the desired pattern to be achieved. For instance, we will assume in this case that we need to generate a flat-top pattern with the minimal ripples in the main lobe and with symmetric side-lobe level of -10dB and a HPBW of 40° as shown in the mask of Fig 3.11. This desired pattern is defined by choosing the number of lobes in the pattern, which equals the number of elements in the array minus one, and the desired height for each lobe of them which determines the required side lobe topology and the envelope of the main lobe. As the number of lobes increases, the width of each lobe will decrease and so one can achieve more flexibility in shaping the pattern. For example, the pattern in our case needs to achieve a sharp transition between low side-lobe values to a high value at the main lobe. This sharp transition needs some flexibility by increasing the number of lobes in the pattern. However, increasing the lobes means the increase of the number of elements which is a drawback for this design as the most compact possible design is required to save the size, weight, and cost of the final imaging system. In this example, the heights of the side lobes are chosen at a -10dB level below the heights of lobes in the main lobe region.

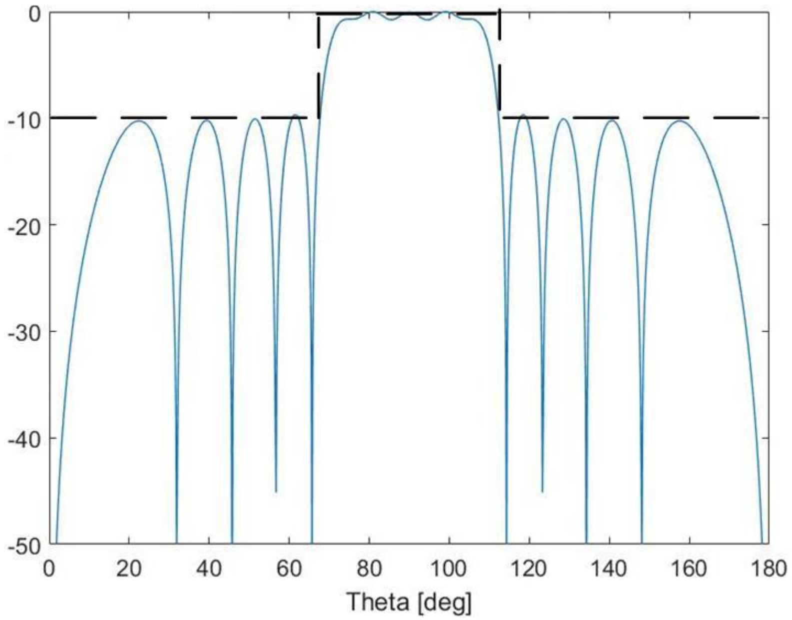

Figure 3-11 The mask of the desired flat-top pattern at SLL of 10dB to be synthesized.

The next step is to synthesize an initial pattern to start the iterations from it until the desired pattern is achieved. From experience, it was proven that this initial pattern doesn't have to be very close to the desired pattern for the iterative process to converge. So, a simple initial pattern can be synthesized using the Schelkunoff method by determining the number and locations of nulls in that pattern. After starting the iterations, if the new patterns are discovered not to be converging to the desired pattern, then the choice of the number of the roots and their locations has to be redefined. For instance, 13 roots were chosen for our case after several trials where four of them lies in the required main lobe region. The resulting starting pattern with this choice is shown in Fig 3.12.

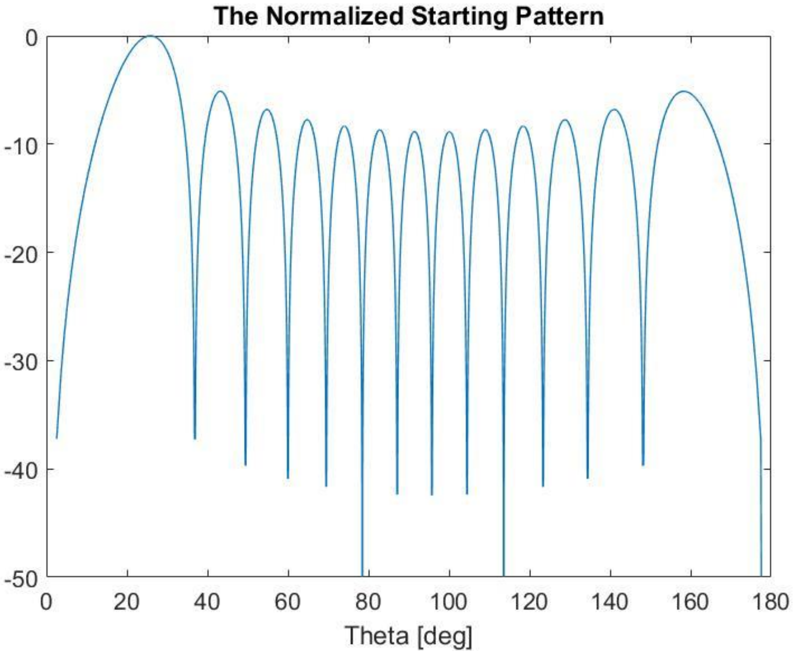

Figure 3-12 The starting pattern for the iterative process showing 13 lobes and 13 nulls obtained by a 14-element array.

Then, a linear perturbation of the roots' locations of the starting pattern on the unit circle is applied, taking into consideration the required lobe heights. This perturbation corresponds to an angular shift in the location of each root on the unit circle. To calculate the required perturbation in each iteration, the algorithm uses the following equation [45]

$$\frac{AF({z_m}^p) - AF_0({z_m}^p)}{AF_0({z_m}^p)} = \frac{\delta C}{C_0} - j\sum_{n=1}^{N-2} \frac{{z_n}'}{{z_m}^p - {z_n}'}\delta\psi_n \tag{3.8}$$

where $AF(z_m^p)$ is the height of the mth lobe in the desired pattern, $AF_0(z_m^p)$ is the corresponding lobe's height in the initial pattern and $(\delta\psi_n)$ is the perturbation that should be applied on the nth root location. So, with the goal of decreasing the error between the initial pattern and the desired pattern, this equation is calculating the required roots' perturbations. Now, the roots locations on the unit circle (ψ_n) will be perturbed angularly using [45]

$$\psi_n|_{iteration\ k+1} = \psi_n + \delta\psi_n|_{iteration\ k} \tag{3.9}$$

resulting in the perturbation of the AF's roots (z_n) by [45]

$$z_n = z_n' e^{j\delta\psi_n|_{iteration\ k}} = z_n'(1 + j\delta\psi_n|_{iteration\ k}) \tag{3.10}$$

This perturbation gives new values for the roots that can be substituted in (3.7) and a new pattern is plotted. If the resulting pattern is not acceptably close enough to the desired one, it can be used as a new starting pattern and the same perturbation process is repeated. It has been shown that these iterations converge rapidly to the desired pattern. For instance, the new pattern achieved after the first iteration in this example, depicted in Fig 3.13, shows a significant change when compared to the initial pattern in the way of achieving the desired pattern. Seven iterations were made from the starting pattern to achieve the required pattern as shown in Fig 3.14 (a), where the final iteration representing the desired pattern is shown in Fig 3.14 (b).

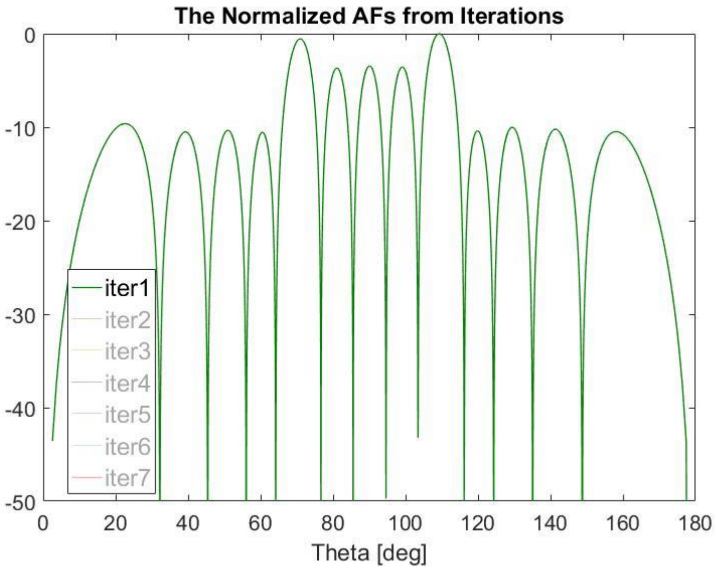

Figure 3-13 The resulting pattern after the first iteration from the starting pattern of Fig 3.12.

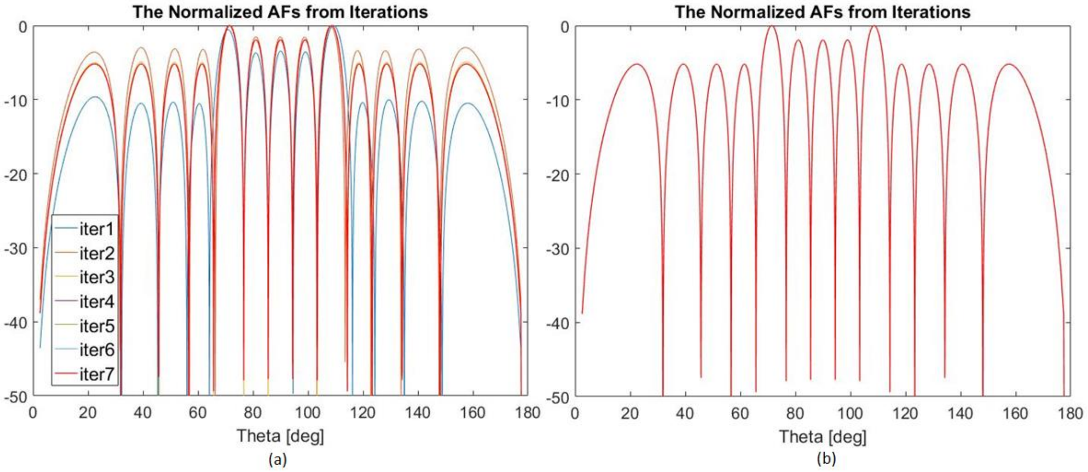

Figure 3-14 (a) The resulting normalized AF of each iteration from the starting pattern to the desired pattern (b) The last iteration showing the desired pattern.

Up to this point, this technique gives a powerful control on the height of each lobe including the main lobe, but, it does not give any control on customizing the shape of this main lobe, it can only be a single narrow lobe. The same author, Elliott, then extends his technique in [49] to be able to shape the main beam. This shaping is done by dealing with the main lobe as a combination of some of these narrow lobes, whose heights were chosen in the mask of the desired pattern from the first step, to follow a certain desired contour. However, these lobes are separated by deep nulls that need to be filled. This objective can be achieved by radially shifting the roots that correspond to these nulls from the unit circle, and as mentioned earlier, only the roots that lie on the unit circle contribute to the nulls of the pattern.

To investigate the effect of radially shifting a root from the unit circle, only one root that corresponds to the first null in the main lobe of the desired pattern is shifted as shown in Fig 3.15 and the new pattern is plotted in Fig 3.16. The resulting pattern shows how the corresponding null to the shifted root is filled. Using the same idea for the other three roots that correspond to the remaining three nulls in the main lobe, the final required flat-top pattern with SLL of 10dB will be achieved as shown in Fig 3.17.

The required shift for each root to achieve the desired envelope for the main lobe can be calculated from [49]

$$|AF(z_m)| = \left| C_1 b_m \prod_{1}^{N-1} (z_m - z_n) \right| = Envelope \tag{3.11}$$

where $|AF(z_m)|$ is the new height of the AF at the location of the mth that will be shifted, (b_m) is the distance by which the root should be shifted from the unit circle, and (Envelope) represents the value of the desired envelope at this location. Knowing the envelope's value, we can solve (3.11) to calculate the required shifting distance. It was noticed that this null filling process is affecting the SLL of the resulting final pattern when compared to that of the last iteration step before radially shifting the roots. This difference can be noticed by comparing the SLL in Fig 3.14(b) before shifting the roots and in Fig 3.17 after shifting them.

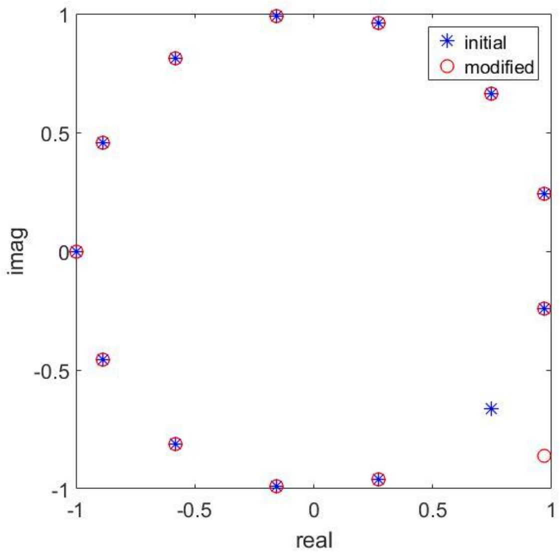

Figure 3-15 The Schelkunoff unit circle showing the final locations of the roots of the desired pattern (in blue) and one of them is shifted outwards the unit circle.

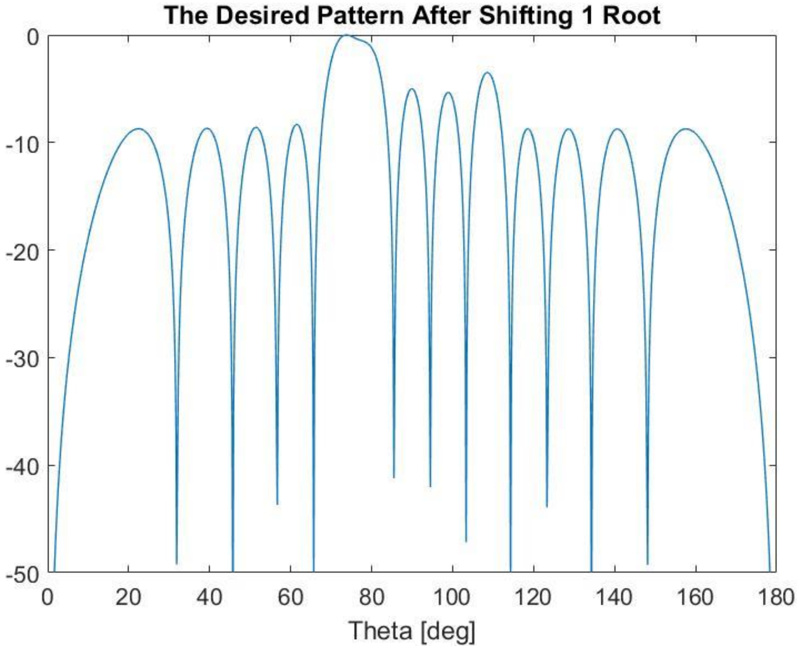

Figure 3-16 The resulting pattern after shifting the root that corresponds to the first null in the main lobe outwards the unit circle showing how this null is filled.

This effect can be explained by returning to (3.7). This equation shows that the magnitude of the AF at any observation angle (θ) depends on the distance between the corresponding value of (z) and each one of the roots. So, when any of the roots' location is shifted, the distance between it and (z) will change affecting the magnitude of the (AF) at all the observation angles. By considering this effect, the SLL was chosen in the desired mask to be achieved from the iterations at a different level (-5 dB) than the required value (-10 dB), so the SLL in the final pattern after shifting roots will be at -10dB.

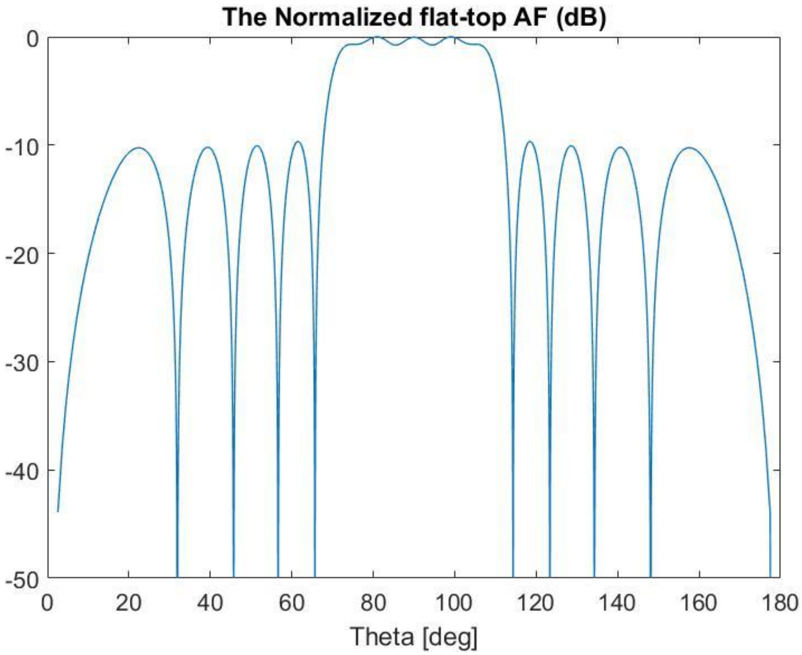

Figure 3-17 The final obtained pattern after the null-filling process (in dB) with SLL of 10dB.

The final step is to extract the required excitation coefficients for each element in the array to generate this pattern. This step is achieved by using the polynomial expression of the AF of this non-uniform array of N-equally spaced elements [43]

$$AF = \sum_{n=1}^{N} a_n z^{n-1} = a_1 + a_2 z + a_3 z^2 + \cdots + a_N z^{N-1} \tag{3.12}$$

and equating that with the form of equation (3.7) that contains the roots of the AF. By knowing the roots of the final pattern, this polynomial can be solved to get the required excitations coefficients.

It's important to notice that the resulting pattern after shifting the roots out of the unit circle depends only on the magnitude of the shift, and there is no any difference between shifting a root inside or outside the unit circle. Thus, we have for each root two available shifting options giving a total number of (2^M) available shifting solutions that will provide the same pattern, where (M) is the number of the roots to be shifted. Each solution gives different excitation coefficients for the array elements to generate the same pattern. However, a judicious decision should be taken to choose the best shifting scheme. It is observed that when all the roots are shifted in the same direction, like the case shown in Fig 3.18(a), the resulting excitation coefficients are all real but asymmetric. While shifting the roots interchangeably inside and outside the circle, shown in Fig 3.18(b), results in symmetric but complex excitation coefficients. The resulting excitation coefficients from each case to generate the flat-top pattern with SLL 10dB are presented in table 2.

Obviously, the real excitation coefficients are easier to be implemented in the feeding network as all the excitation phases will be either 0° or 180°, so no complex phase shifting designs are required. Also, when simulating this array in the EM solver, the same pattern is expected to be generated using either case of the excitations. However, results depicted in Fig 3.19 shows that the real and asymmetric -excitation coefficients result in an asymmetric pattern. The explanation of this effect is that the mutual coupling that occurs between the elements is also asymmetric in this case because the excitation amplitudes are asymmetric. For this reason, the complex and symmetric excitation coefficients were chosen instead.

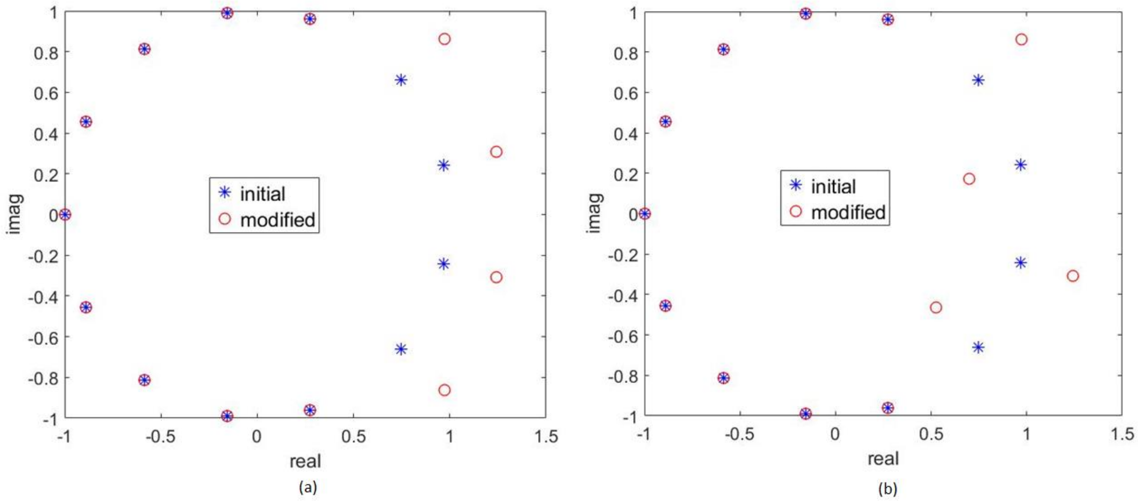

Figure 3-18 The Schelkunoff unit circle showing two available root shifting schemes for the same pattern (a) shifting all the roots in the same directions, for example, outside the circle, and (b) shifting the roots interchangeably inside and outside the circle resulting in different excitation coefficients.

Table 2

The resulting symmetric and asymmetric excitation coefficients of the 10dB SLL.

Element #	The Asymmetric Case	The Symmetric Case
1	1.0000	1.0000 + 0.0000i
2	-0.7196	0.0905 - 0.2504i
3	-0.3534	-0.1560 - 0.3550i
4	0.1557	-0.2408 - 0.1292i
5	0.5174	-0.0283 + 0.4374i
6	0.4079	0.3823 + 1.1278i
7	-0.1804	0.7102 + 1.6020i
8	-0.7932	0.7102 + 1.6020i
9	-0.7949	0.3823 + 1.1278i
10	0.1054	-0.0283 + 0.4374i
11	1.5394	-0.2408 - 0.1292i
12	2.6908	-0.1560 - 0.3550i
13	2.8877	0.0905 - 0.2504i
14	2.7689	1.0000 + 0.0000i

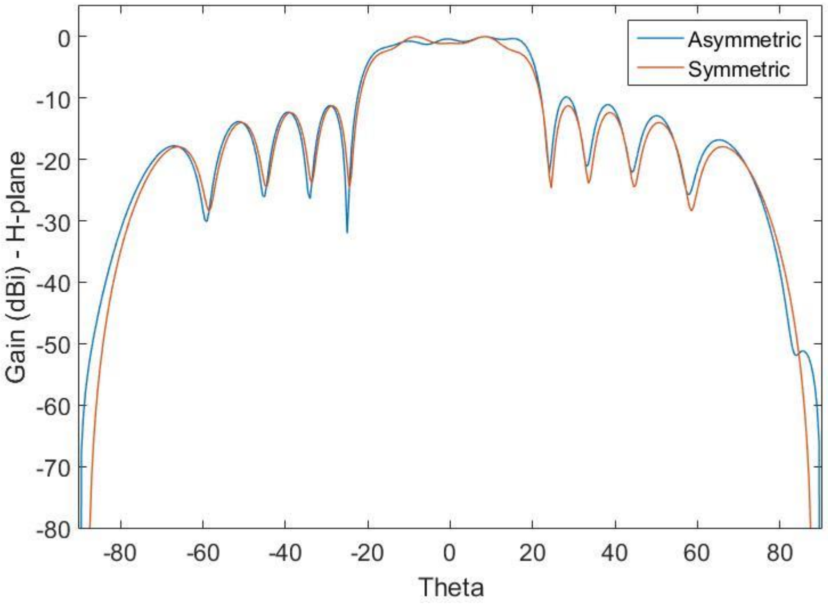

Figure 3-19 The actual radiation pattern of the 14-element 10dB linear array excited by (a) the real asymmetric coefficients, and (b) the complex symmetric coefficients.

In summary, a powerful pattern synthesis method is utilized to achieve the required flat-top pattern. This technique relies on an optimization algorithm that starts from an initial pattern until the desired one is achieved, with steps that are summarized in the flowchart shown in Fig 3.20. It was proven that this initial pattern converges rapidly to the desired one regardless how close they are from each other. Therefore, this starting pattern was synthesized using the Schelkunoff method which requires only choosing the number and locations of nulls in the pattern.

However, as in any design problem, the process of achieving the required pattern encounters some tradeoffs. For example, to decrease the HPBW with the same number of elements in the array, the SLL will decrease also. Keeping in mind that, for this specific design, it is better to have a higher SLL to minimize the radiation directed outside the desired FOV. Otherwise, to maintain the SLL, the number of elements has to be increased. Also, the ripples can be controlled through the null-filling process by changing the radial shift of each root. However, decreasing the peak-to-peak ripples affects the flatness of the main beam and the sharp transition between it and the side lobes. Several optimization techniques were presented to reduce the peak to peak ripples like the one by Orchard in [50].

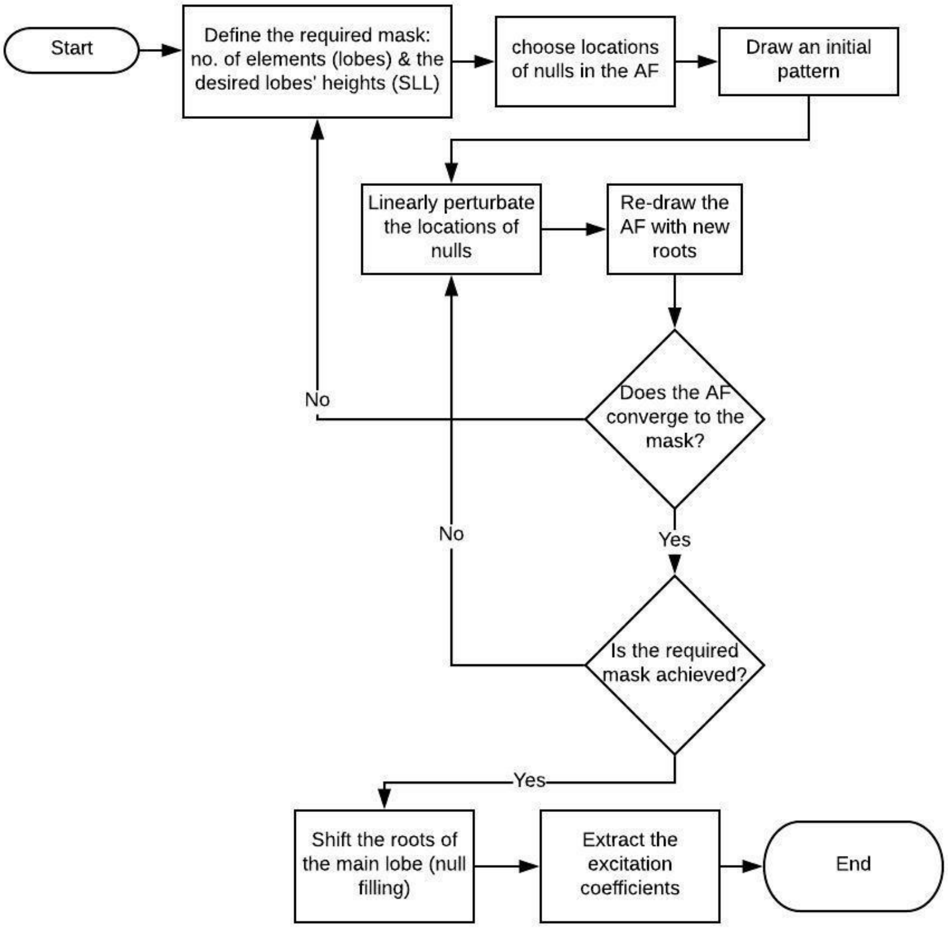

Figure 3-20 A flowchart of the utilized optimization algorithm to synthesize any desired radiation pattern.

Three versions of this 14-element flat-top non-uniform array of dipoles for three different SLLs at 10dB, 20dB, and 30dB are synthesized and the corresponding excitation coefficients are presented in tables 3, 4, and 5 respectively. For example, the obtained pattern from the full-wave simulator of the SLL of 20dB case is shown in the figures from 3.21 to 3.23. By investigating this pattern, we can notice that the flat-top pattern is achieved as required in one plane. However, the orthogonal plane still has the wide beamwidth as that of the linear array. The required pattern should possess both the flat-top pattern in one plane and the fan beam in the orthogonal plane. To achieve that, a two-dimensional array was created with the uniform phased 64-element array in one dimension generating the fan-beam, and the non-uniform 14-element array in the other dimension generating the flat-top pattern.

Thus, the final design comprises a 14×64 element two-dimensional array of half-wavelength dipoles at a spacing of d = λ/2, as shown in Fig 3.24. A comparison between the radiation patterns of the three designs with SLLs of 10dB, 20dB, and 30dB respectively along with the uniform 64-element linear array is shown in Fig 3.25. The HPBW, gain, and main lobe ripples of each design are presented in table 6. From the comparison, it’s clear that, for the same number of elements, decreasing the HPBW comes at the cost of decreasing the SLL.

Table 3

The complex symmetric excitation coefficients of the 10dB SLL array.

Element #	Excitation Amplitude	Excitation Phase (°)
1	1	0
2	0.2663	-70.13
3	0.3877	-113.72
4	0.2733	-151.78
5	0.4383	93.7
6	1.19	71.27
7	1.752	66.09
8	1.752	66.09
9	1.19	71.27
10	0.4383	93.7
11	0.2733	-151.78
12	0.3877	-113.72
13	0.2663	-70.13
14	1	0

Table 4

The complex symmetric excitation coefficients of the 20dB SLL array.

Element #	Excitation Amplitude	Excitation Phase (°)
1	1	0
2	0.91	-17
3	0.62	-62.74
4	0.6	-137.9
5	0.674	132.38
6	1.938	76.95
7	3.259	64.94
8	3.259	64.94
9	1.938	76.95
10	0.674	132.38
11	0.6	-137.9
12	0.62	-62.74
13	0.91	-17
14	1	0

Table 5

The complex symmetric excitation coefficients of the 30dB SLL array.

Element #	Excitation Amplitude	Excitation Phase (°)
1	1	0
2	1.718	-9.26
3	1.378	-34.178
4	0.92	-119.38
5	1.2	155.93
6	2.948	82.87
7	5.48	64.71
8	5.48	64.71
9	2.948	82.87
10	1.2	155.93
11	0.92	-119.38
12	1.378	-34.178
13	1.718	-9.26
14	1	0

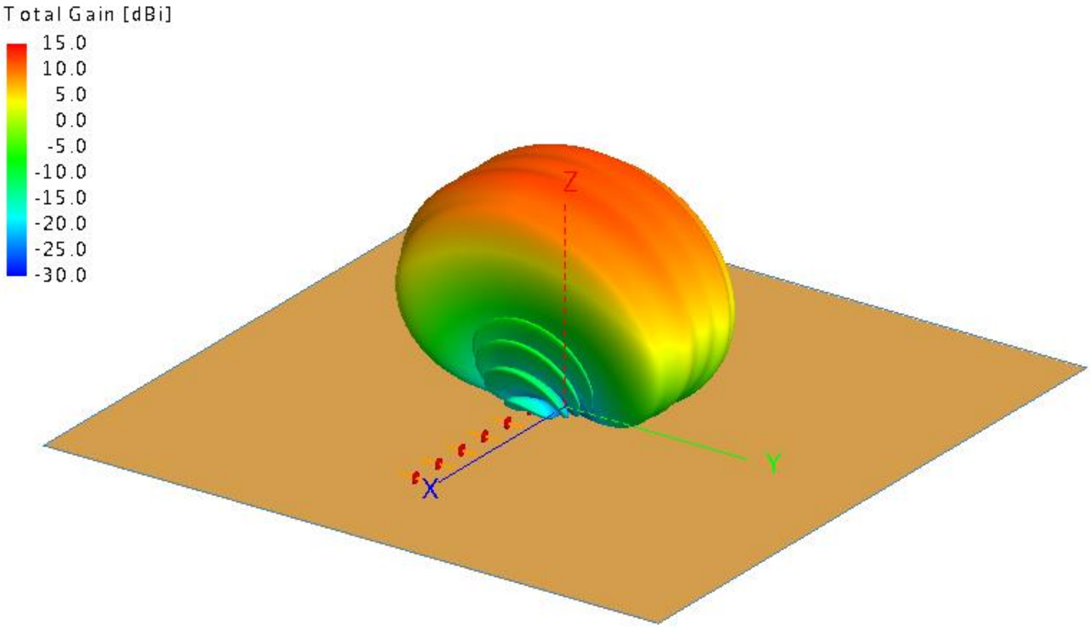

Figure 3-21 A 14-elements one-dimensional array with a flat-top pattern and SLL of 20dB at a height of λ/4 above a PEC plane showing the 3D radiation pattern of the array at an angle $\theta_0 = 0°$.

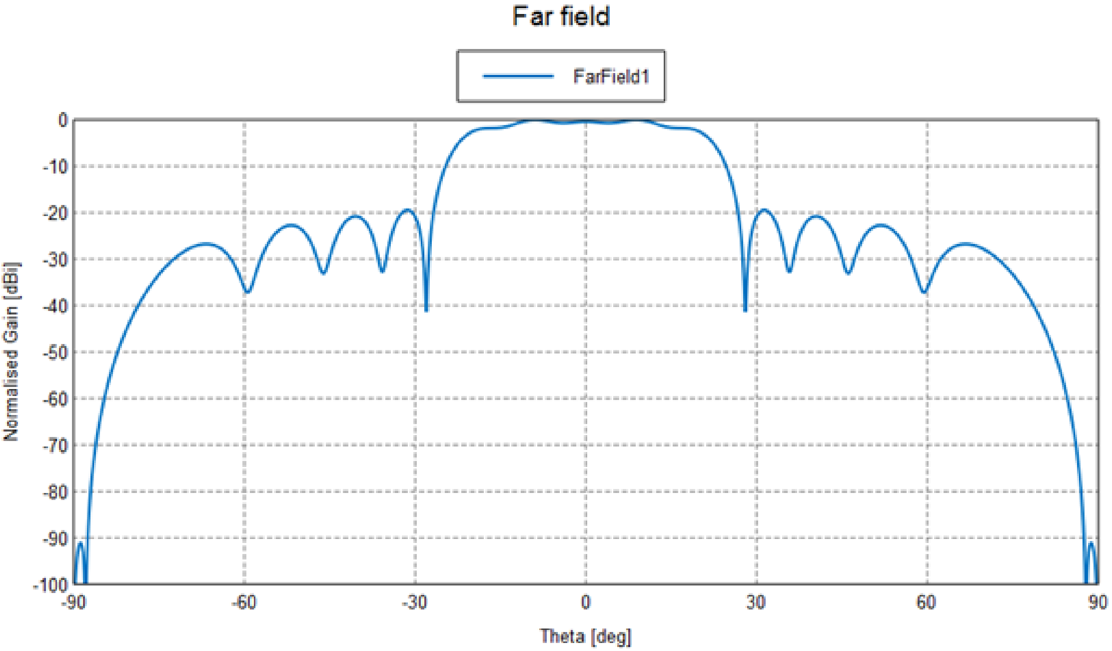

Figure 3-22 The *H*-plane of the radiation pattern of a 14-element flat-top array with SLL of 20dB.

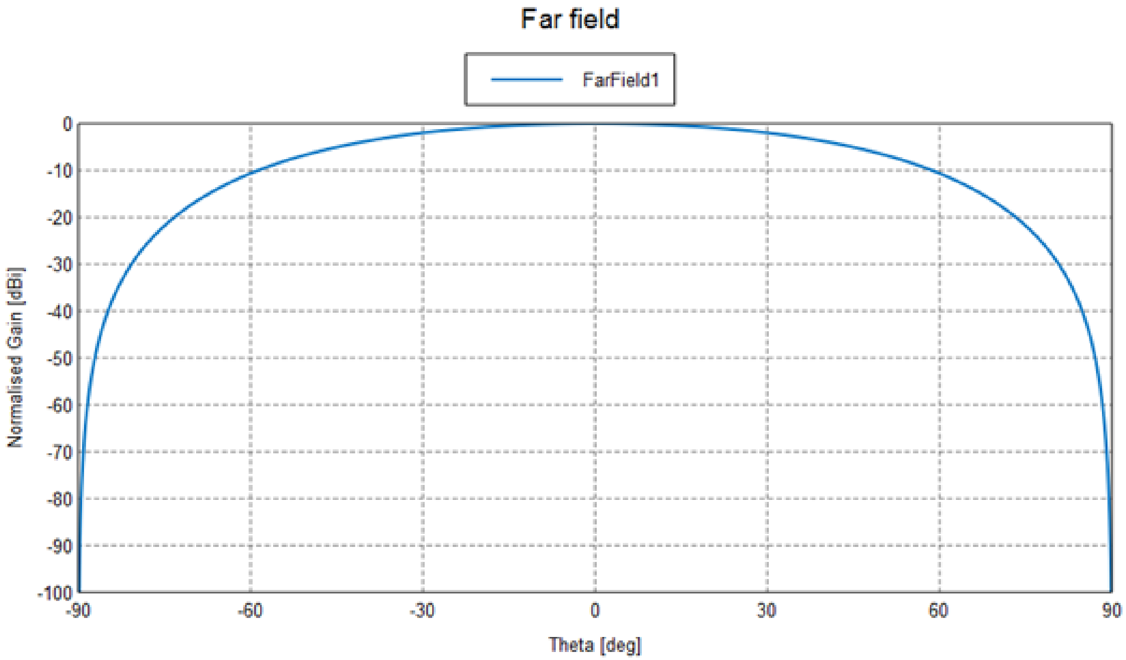

Figure 3-23 The *E*-plane of the radiation pattern of a 14-element flat-top array with SLL of 20dB.

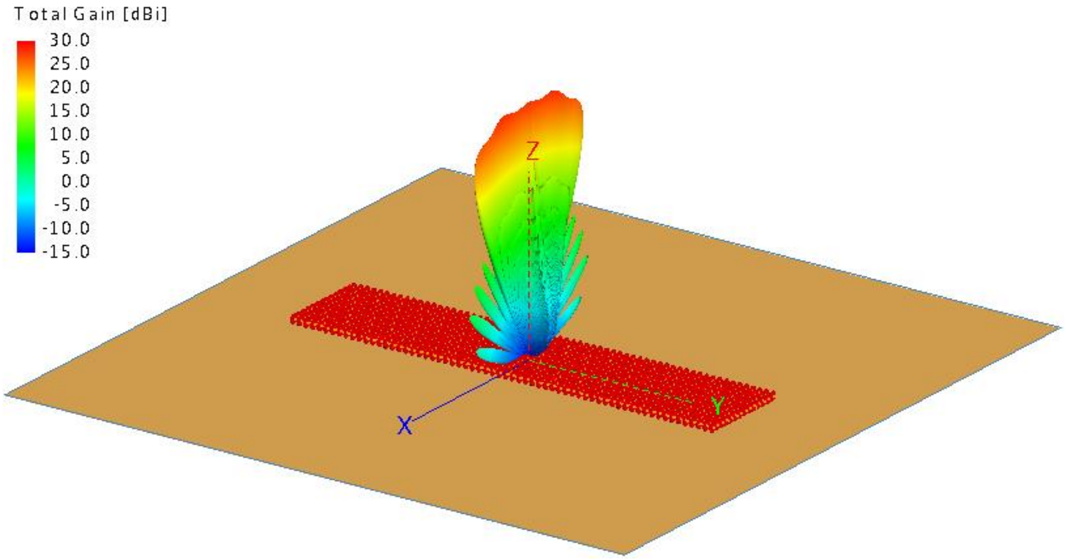

Figure 3-24 A 14×64-elements two-dimensional array with a flat-top pattern and SLL of 20dB at a height of λ/4 above a perfect PEC plane showing the 3D radiation pattern of the array at an angle $\theta_0 = 0°$.

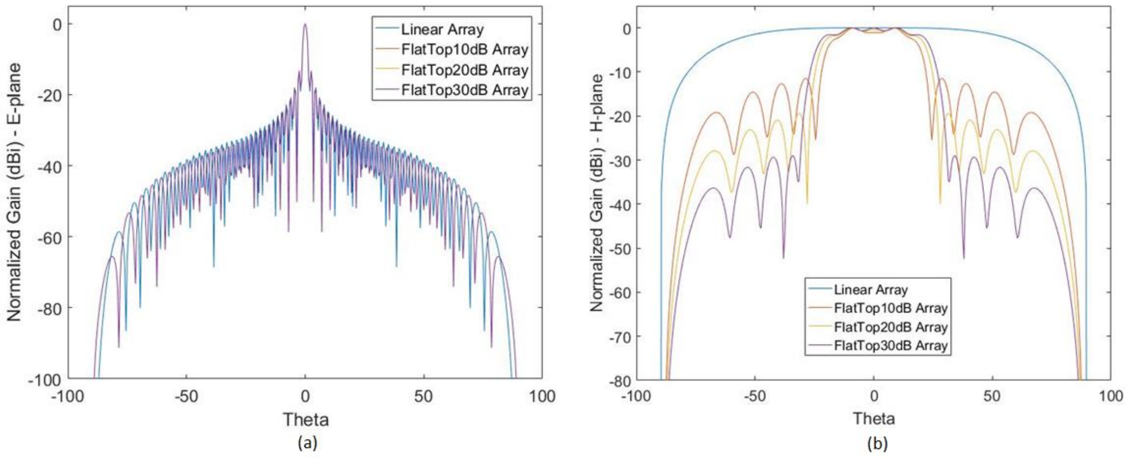

Figure 3-25 A comparison between the radiation patterns of the 14x64 elements flat-top arrays with SLLs of 10dB, 20dB, and 30dB along with the pattern of the 64-element uniform linear array (a) The *E*-plane, (B) The *H*-plane.

Table 6

A comparison between the HPBW, gain, and the ripples of three flat-top array designs at SLLs of 10dB, 20dB, and 30dB.

	SLL = 10dB	SLL = 20dB	SLL = 30dB
HPBW (E-plane)	1.43°	1.43°	1.43°
HPBW (H-plane)	35°	41.16°	44.9°
Gain [dBi]	27.5	28.13	27.73
Ripples (peak to peak)	2.25	1.9	1.6

Considering the beam curvature problem that was noticed in the linear array design with tilting the beam to larger angles, the flat-top antennas are seen to possess the same curvature, as shown in Fig 3.26 and Fig 3.27, with the only difference of being limited to a narrower beamwidth. This fact is due to having the same 64-elements phased array in one dimension of the flat-top antenna that is responsible for tilting the beam as in the linear array design.

Finally, a comparison between the generated beams from the uniform 64-element linear array and the 14×64 elements flat-top array is shown in Fig 3.27. This figure shows a top-view for the beam of each antenna design as it is scanning the FOV.

Referring to Fig 3.6, we can see that the main required objective from the flat-top antenna is achieved as it is focusing its radiation only within the desired FOV dimensions. Mitigation of the interference that may occur from any objects outside the FOV is achieved.

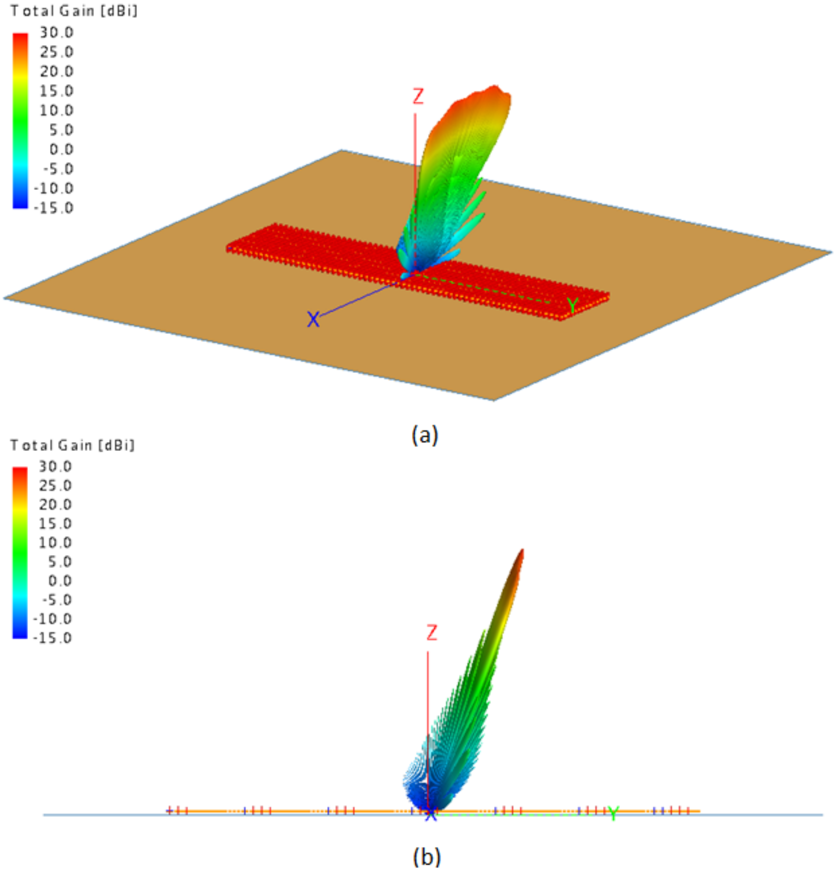

(a)

(b)

Figure 3-26 The 3D radiation pattern of the 14×64-elements flat-top array with SLL of 20dB at a scanning angle of $\theta_0 = 20°$ from (a) the isometric view, (b) a side view.

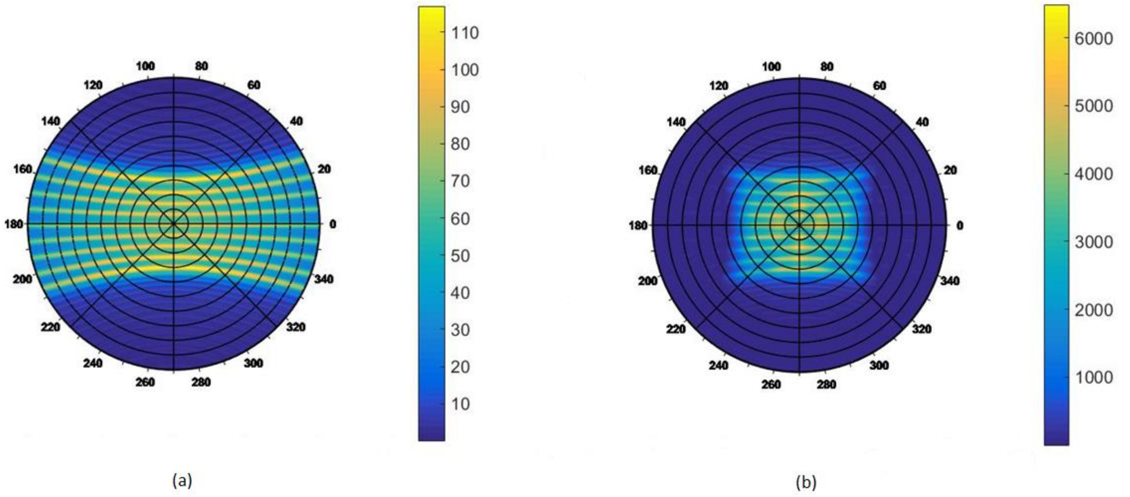

Figure 3-27 A top-view of the beams generated by (a) the uniform linear array, (b) the flat-top array at different scanning angles between -20° and 20°.

3.2.3 A Comparison with the Pencil-Beam Scanning Technique

A brief comparison between the previously discussed designs and a simple design for a pencil-beam scanning technique is presented to illustrate the advantages that the Fourier-slice theorem has offered. The pencil-beam scanning technique depends on using a very narrow beam, namely a pencil beam, to scan a strip of the FOV pixel-by-pixel, and then the beam travels to the next strip to scan it again, and so on. For a high spatial resolution imaging with this technique, this beam should be as narrow as possible to increase the number of pixels being scanned at each strip. To achieve such a narrow beam, one method is to use a square array consisting of two uniform linear arrays on both dimensions, so the resulting radiation pattern will exhibit a fan beam pattern in both *E*- and *H*-planes.

For a fair comparison between the previous designs and the pencil-beam case, the same spatial resolution from all designs is to be achieved. The 64-element uniform linear array that was discussed previously can be used to construct a square array of 64 elements in both dimensions, as shown in Fig 3.28, that has the same spatial resolution. The radiation pattern of this array will exhibit the same fan beam pattern of the 64-element uniform linear array in both *E-* and *H-* planes as shown in Fig 3.29 in comparison with the radiation pattern of only the linear array. For more clarification, a comparison between the HPBW and gain of both arrays is given in table 7.

Table 7

A comparison between the HPBW and the gain of the 64×64 elements square array and the 64 elements uniform linear array.

	64×64 square array	64-element Linear Array
HPBW (E-plane)	1.46°	1.46°
HPBW (H-plane)	1.48°	120°
Gain [dBi]	41.11	22.97

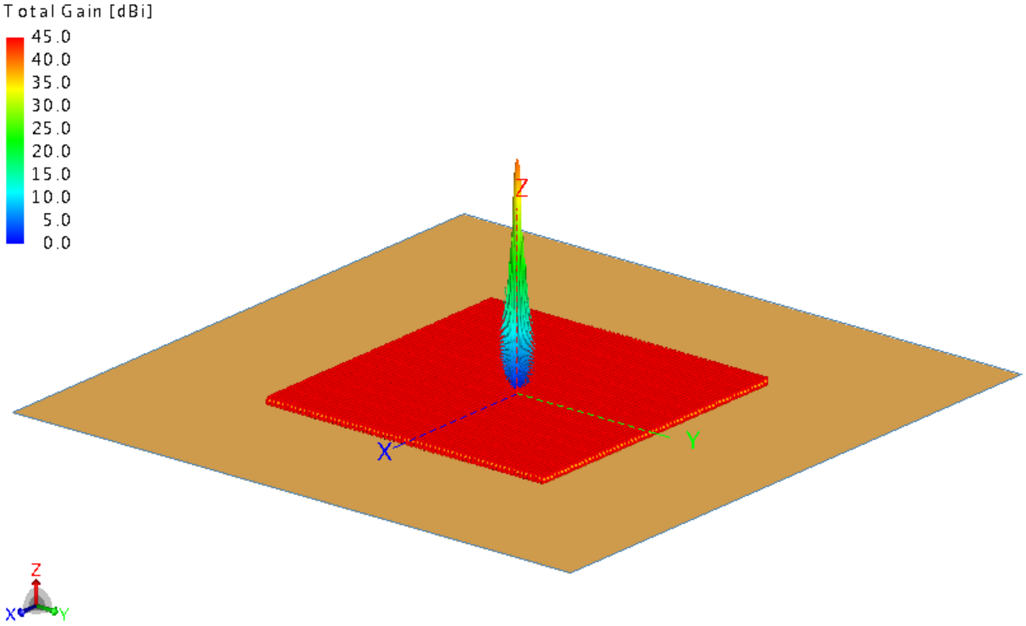

Figure 3-28 A 64×64 elements square array with a pencil beam pattern at a height of λ/4 above a perfect PEC plane showing the 3D radiation pattern of the array at an angle $\theta_0 = 0°$.

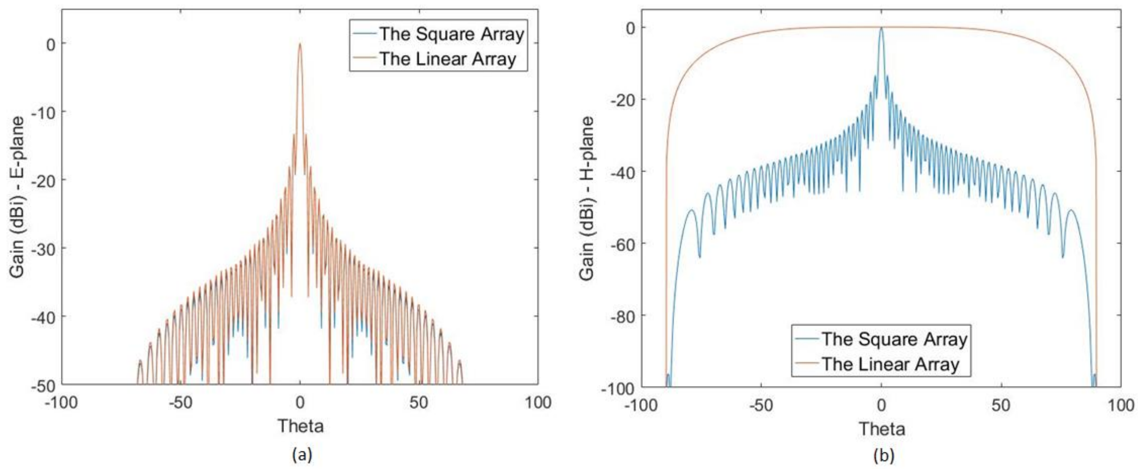

Figure 3-29 A comparison between the radiation patterns of the 64x64 elements square array and the pattern of the 64-element uniform linear array (a) The *E*-plane, (b) The *H*-plane.

The previous discussion shows that using the Radon transform imaging technique that depends on illuminating a complete strip of the FOV at a time, instead of scanning it pixel-by-pixel, allows the usage of much more compact array designs that generates a fan beam at one plane and a relatively wider pattern on the other plane with HPBW equals the width the desired FOV. So, instead of using 64×64 = 4096 elements for a pencil-beam array, we can squeeze this number to only 14×64 = 896 elements, with a factor of almost 4.5!

3.3 Digital Beamforming and Simplification of the Feeding Network

Recently, the interest in digital beamforming techniques has increased as a potential method to enhance the efficiency of wireless communications [43]. This is because of the ability of these systems to adaptively direct the beam in the direction of the intended user and null the beam at the directions of other interferers. While this process is being done using advanced digital signal processors (DSP) with the help of different computational algorithms. A brief comparison between digital beamforming and the conventional phased array techniques is discussed.

The digital beamforming does not include a physical steering of the radiated beam as the case of the phased arrays. Instead, the beam steering is done computationally in the DSP part of the system through different algorithms that have been developed for this purpose. The array in the digital beamforming requires a separate analog-to-digital (ADC) converter for each antenna element to down-convert the signal to the base band (refer to Fig 3.30 (a)), so it ends up having as many digital streams as the number of elements in the array. Then, these digital streams are summed up with the appropriate weighting factors and phase shifts to construct the composite signal. While in the analog beamforming situation in phased antenna arrays, the received signals from each element are weighted and phase-shifted with the RF front end part of the system, and the signals are added to one composite signal which is converted by a single ADC converter to the base band, as shown in Fig 3.30 (b). The same idea applies in the case of transmitting the signal.

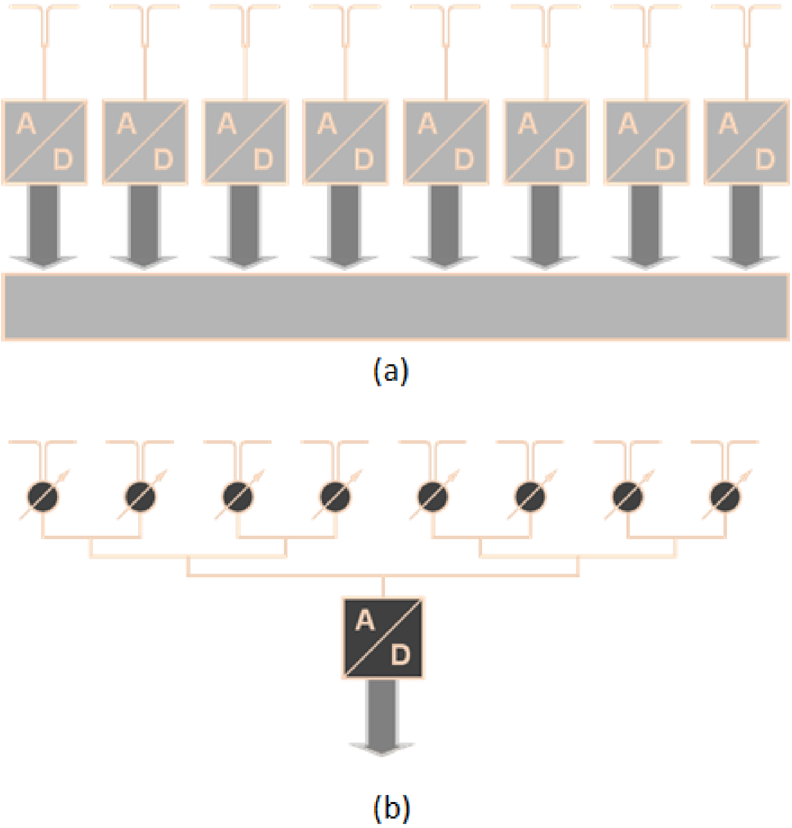

Figure 3-30 A comparison between the required transceivers in (a) digital beamforming systems, and (b) analog beamforming systems.

The major advantage of digital beamforming is that it allows the system to get rid of complex analog transceivers in the RF front end that are required to generate the weights or excitations for each antenna element. However, in digital beamforming, the system requires as many transceivers as the number of antenna elements, and an accurate real-time calibration for each one of them. Also, it needs powerful DSP to be used to be able to support the computationally intensive processes of the beamforming.

3.4 Summary

In a summary, two phased antenna array designs were presented in this chapter. The first design comprised a uniform linear array of 64-elements generating a highly directive fan beam but with the disadvantage of a wide beamwidth in the *H*-plane. Also, this beam suffers from significant curvature as it is tilted to greater angles introducing computational errors in the reconstruction of the image due to its failure to achieve a perfect parallel beam projection imaging as assumed in the post processing. However, this design has the advantage of using a compact array of only 64 elements that exhibits an almost uniform gain in the desired FOV. The second design provides solutions for the previous drawbacks. A flat-top pattern is generated computationally using an optimization algorithm that perturbs the locations of the nulls in a starting pattern until the desired pattern is achieved and the required excitation coefficients are extracted. The structure of this array contains 14×64 elements two-dimensional array, with non-uniform amplitude excitations along the *H*-plane. As it will be shown in the next chapter, the flat-top antenna array provides superior imaging performance by mitigating the interference from sources outside the FOV.

Both designs are examined using simulations at 300 GHz of a phantom object representing the target and the results will be presented in the next chapter to compare the efficiency of them. But before proceeding to the simulation results, a quick overview on the technique used to model this imaging system and to simplify performing these simulations will be presented.

CHAPTER 4

SIMULATION TECHNIQUES AND RESULTS

In this chapter, we compare the imaging performance of the two antenna array designs presented in the previous chapter, hence the linear phased array and the flat-top beam antenna array. Computational imaging is particularly demanding numerical problem due to the electrically large dimensions of the model. As such, we discuss a suitable simulation platform that can test the ability of each design to correctly implement this technique and reconstruct the image of targets in the FOV.

4.1 Analysis of the Modeling Method

A conventional simulation setup will comprise the antenna array along with a phantom object (e.g. a sphere) representing the target that could be either inside or outside the FOV, as shown in Fig 2.5 (chapter 2). However, this setup needs a significant simulation time to finish all the required simulations for the construction of each image. To appreciate the required number of simulations in this algorithm, we need to consider that the simulation process needs to be repeated for N beam scanning angles. This process is then repeated for M antenna rotation angles needed for the Radon transform as discussed earlier. As such, the field propagation and scattering problem needs to be repeated a total of N×M times which can be extremely time-consuming for imaging systems with multiple antennas.

Specifically, in our case the required FOV to be imaged has dimensions of 40°×40° extending from -20° to 20°. For a high-resolution image, the beam scanning step is determined by the beamwidth, which is chosen in this simulation at 0.5°

resulting in 81 repeats at each antenna projection angle. Moreover, the Fourier slice theorem requires the number of scanning angles at each projection and the number of projections to be close. Thus, 90 projections are done for the antenna from 0° to 180° at a step of 2°. As a result, a total number of 7290 simulations in the full-wave simulator will be required for each image reconstruction. This large number of simulations required for each image reconstruction represents a very computationally intensive algorithm, especially for electrically large targets. As a result, a novel algorithm presented in [51] that can calculate the imaging response of the system accurately is used.

4.2 Modeling of Imaging System Using Conjugate Field Coupling

The main idea of this simulation algorithm is to separate the simulations of the array from those of the target in the full-wave simulator and continue generating the image in a numerical solving environment, e.g. Matlab. Specifically, this simulation algorithm aims to examine a bistatic imaging case, modeled by the beam-forming imaging sensor, the target and a fictitious coupling aperture, as depicted in Fig 4.1. To achieve that, the target is globally illuminated by an incident wave, e.g. plane wave, and the scattered fields from this illumination are being calculated on the aperture using a commercial full-wave Multilevel Fast Multipole Method (MLFMM) solver [52]. A schematic for this step is shown in Fig 4.2. Also, the radiated fields by the antenna array are computed on the aperture as shown in Fig 4.3. Finally, the coupling between both the array radiated fields and the target scattered fields is calculated, which represents the signal that couples to the array's sensors. While, this algorithm assumes that the interaction between the antenna array (the imaging sensor) and the target is negligible.

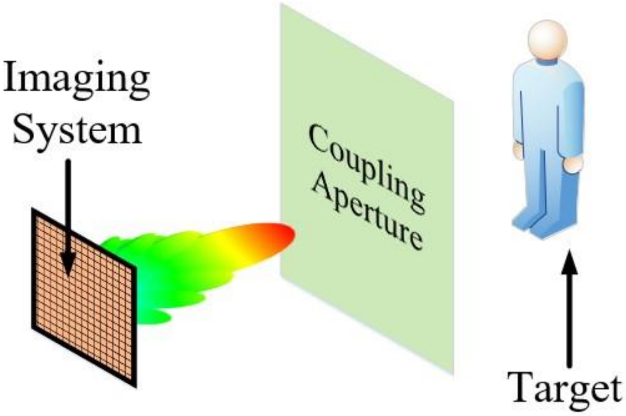

Figure 4-1 The proposed algorithm's schematic configuration. The radiated and scattered fields are recorded on a fictitious aperture, where the conjugate field coupling coefficients are computed (Source: P. C. Theofanopoulos et al., "Modeling of mmW and THz Imaging Systems Using Conjugate Field Coupling," in [51]).

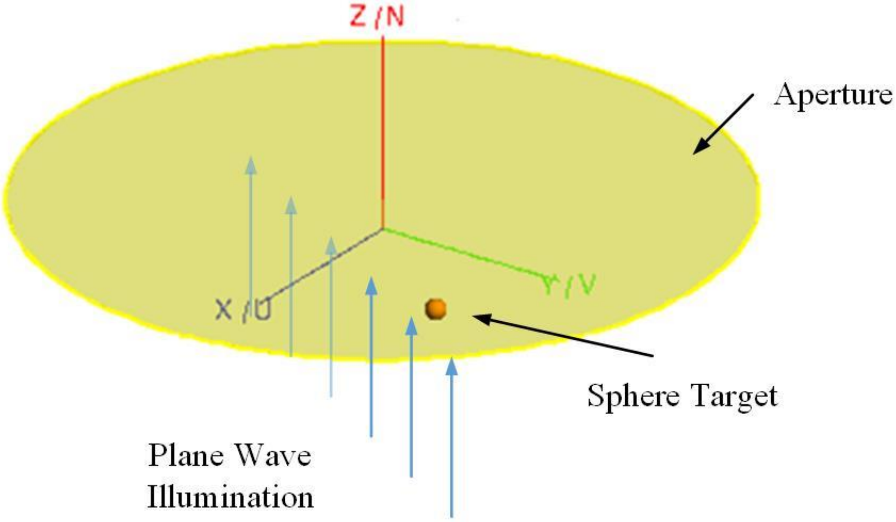

Figure 4-2 The setup of illuminating the target with a plane wave and calculating the scattered fields on the fictitious aperture.

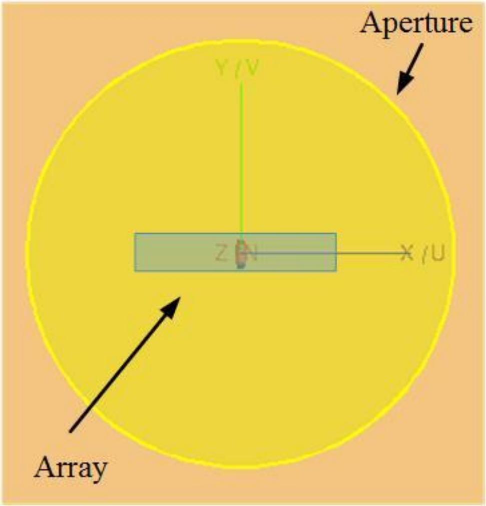

Figure 4-3 The setup of calculating the radiated fields from the array on the fictitious aperture.

The major benefit that can be done is to save the simulation time of repeating this process at all the antenna projection angles, 90 times in this case. This can be achieved by taking advantage of using cylindrical coordinates to mesh the fictitious aperture, the computed fields at a single projection angle of the array can be rotated in Matlab to the different projection angles. This fact can be used to save the valuable simulation time significantly, as the radiated fields by the array are calculated at all the scanning angles only once at a single projection angle. Also, the scattered fields by the target are simulated once. Therefore, the simulation algorithm reduces the computation time 90 times compared to traditional techniques.

In the numerical solver, the Conjugate Field Coupling (CFC) coefficients are used to calculate the coupling between the radiated fields of the antenna array and the scattered fields of the object. The CFC coefficient for the (i,j) direction of a beam scanning imaging system is given by [51]

$$C_{i,j} = \int E_{rad(i,j)} . E^{*}{}_{scat} dS \tag{4.1}$$

where $E_{rad(i,j)}$ represents the beam's (i,j) radiated fields, E_{scat} are the scattered fields from the object, and the $C_{i,j}$ coefficients determine the signal that couples into the array's sensors from the corresponding beam direction representing the projection of the target on the sensor [51]

$$[Projection] = [C_{1,1} \quad \cdots \quad C_{1,m}] \tag{4.2}$$

Finally, after the CFC coefficients are acquired, the filtered back-projection algorithm and the inverse Radon transform are applied in Matlab to the recorded projections to reconstruct the image of the target.

It is important here to notice that the distance of the coupling aperture from the antenna does not affect the results. However, the choice of the field sampling on the coupling aperture is crucial if the aperture is in the near field of the antenna or the target. Referring to Fig 4.4, when the distance (d) from the antenna is within the range $d \leq D^2/2\lambda$; where (D) is the largest dimension in the system which is the diameter of the antenna or the FOV, then the field sampling should be at least $\lambda/2$. Moreover, the size of the coupling aperture itself is directly related to the dimensions of the antenna aperture and the FOV. From Fig 4.4, the diameter of the coupling aperture (L_{CA}) is [51]

$$L_{CA} = L_S + 2d \tan \theta_{sensor} \tag{4.3}$$

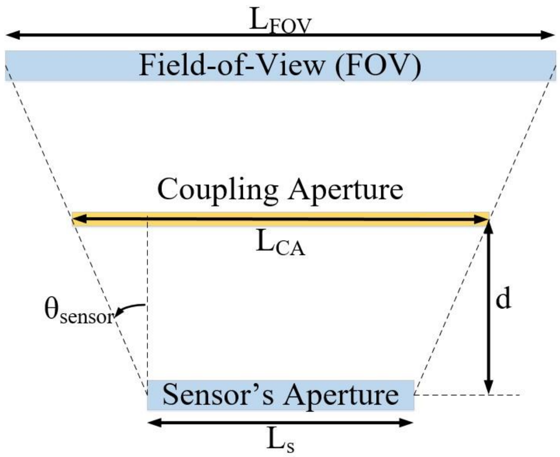

Figure 4-4 The coupling aperture used to record the sensor's radiated fields and the target's scattered fields (Source: P. C. Theofanopoulos et al., "Modeling of mmW and THz Imaging Systems Using Conjugate Field Coupling," in [51])

4.3 A Quantitative Comparison between the Interference Mitigation of the Antenna Array Designs

An essential objective of the following simulations is to construct a comparison between the different antenna designs in a quantitative way. One way to do that is to reconstruct the images of the same object several times at various locations from the center of the FOV to very wide angles outside the FOV with small steps between them and compare these images quantitatively. This comparison can be done in terms of the average power of the reconstructed image of the FOV. Ideally, we expect to see high powers in the cases of the object being inside the FOV and to see nothing if this object is at any position outside the FOV. However, practically, the objects outside the FOV still experience some illumination from the antennas due to the wide beamwidth of the linear array or the side lobes of the flat-top antenna. As a result, even if the object is outside the FOV, like the case shown in Fig 4.5 (a), the reconstructed image in the FOV will not be completely black. However, a distortion of the FOV will occur due to this interferer as shown in Fig 4.5 (b) for a plane wave representing an interferer outside the FOV at 30°. The goal here is to compare the efficiency of each antenna design in terms of decreasing this distortion effect caused by the interferers outside the FOV. The same comparison can also be done in terms of the maximum field value of the reconstructed object's image inside the FOV.

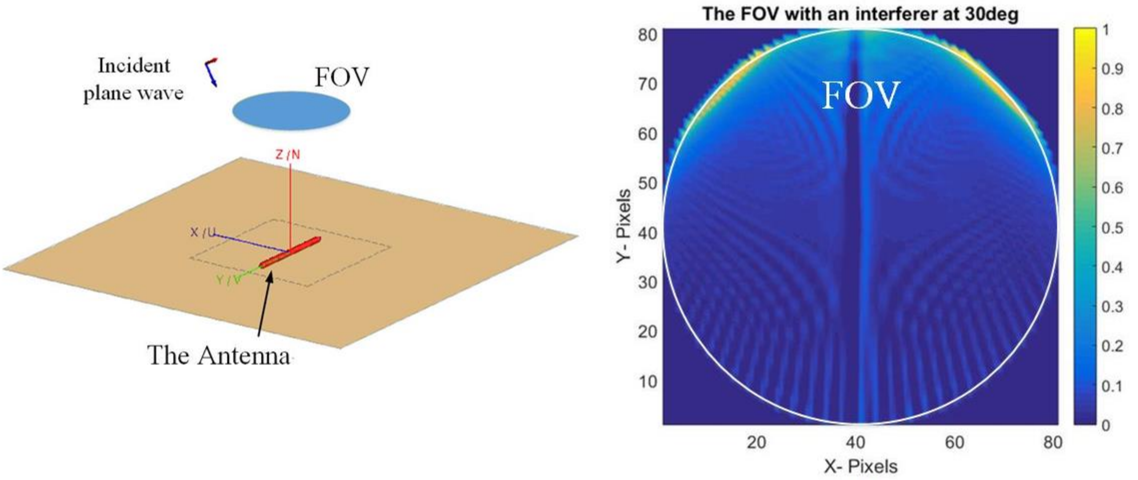

(a) (b)

Figure 4-5 (a) A plane wave representing an interferer outside the FOV at 30°, (b) the reconstructed image of this setup showing how the FOV is distorted due to this interferer.

Because using spheres to perform the image comparisons is computationally intensive, we instead opted for plane waves that illuminate the antenna arrays from multiple view angles. The received signal for a plane wave illumination corresponds to the impulse response of the imaging system. This idea is implemented using 41 plane waves at directions from 0° to 80° with a step of 2°, where the superimposed reconstructed images of all the targets are plotted in Fig 4.6 using the flat-top antenna with a SLL of 20dB.

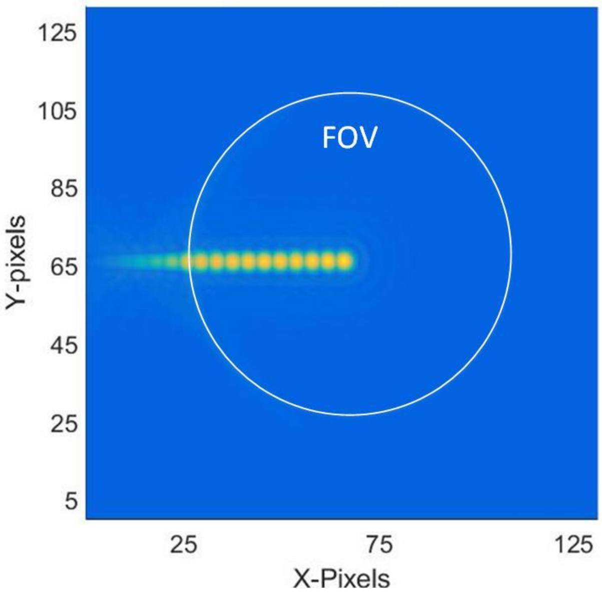

Figure 4-6 A collection of all the reconstructed images for the 41 plane waves, coming from directions that varies between 0° to 80° with a step of 2°, on the same plot.

The comparison results between all the proposed antenna designs are shown in Fig 4.7 and Fig 4.8 for the average power and the maximum field reconstructed inside the FOV for each target from 0° to 80°, respectively. Each comparison is done once with respect to the global maximum value from all the antennas, and once with respect to the local maximum of each array alone.

The difference in the gain between the antennas inside the FOV is clear from the comparison to the global maximum shown in Fig 4.7(a) and Fig 4.8(a). These figures show that the flat-top designs have the highest gain, and so the highest maximum field and average power compared to the linear array. Also, the flat-top antennas have lower gains outside the FOV, which is another advantage for the flat-top antennas allowing it to mitigate the interference from any possible outside interferer significantly.

While comparing the antennas to the local maximum is shown in Fig 4.7(b) and Fig_4.8(b). This comparison reveals the enhancement in the side-lobe level of the flat-top antenna over the linear array is obvious with a difference of almost 20dB between the average power of the linear array and the worst flat-top design of 10dB SLL. These figures can be directly related to the comparison of the radiation patterns of all the antennas shown in Fig 3.25.

One note to be mentioned on these plots is that as we are using cylindrical coordinates, the size of each mesh is not the same, but it is increasing as we go farther away from the aperture center. As a result, the accuracy is getting worse as we go towards more oblique angles. However, the comparison of the average reconstructed power in the FOV is much smoother as it counts for all the values in the FOV and takes the average, not comparing a single value as in the case of comparing the maximum reconstructed field in the FOV.

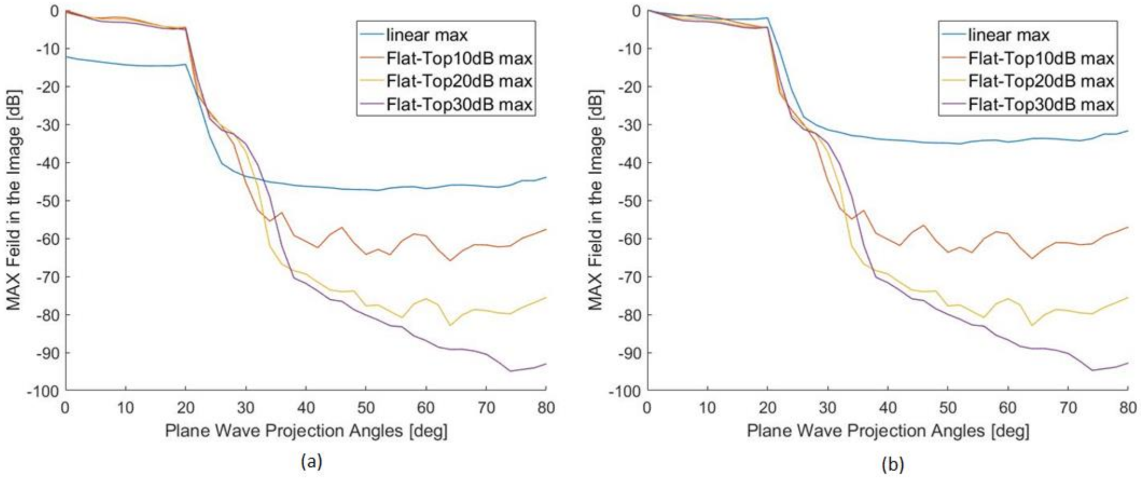

(a)

(b)

Figure 4-7 A comparison between the different proposed antenna designs in terms of the maximum reconstructed field value inside the FOV in the image of each target. Figures are normalized to the (a) global maximum value, and (b) local maximum value.

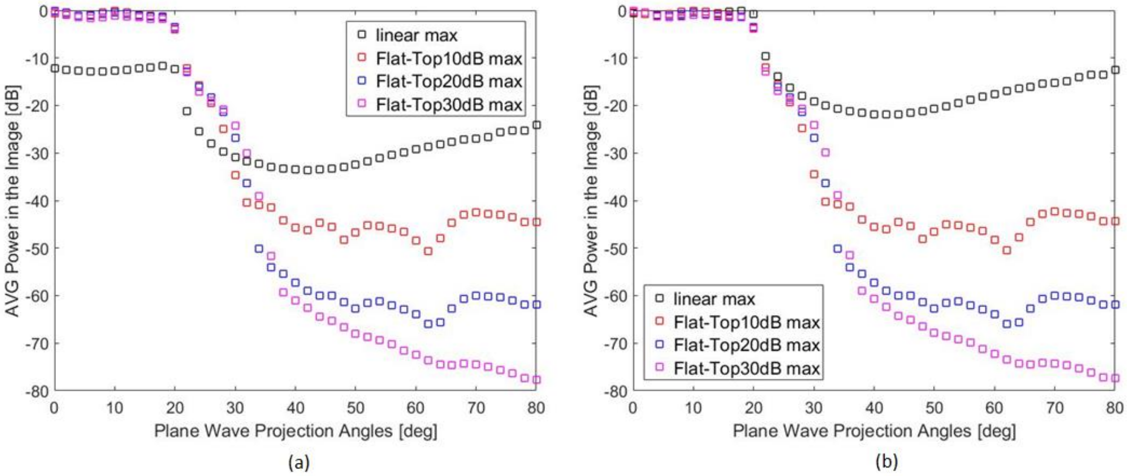

Figure 4-8 A comparison between the different proposed antenna designs in terms of the average reconstructed power inside the FOV in the image of each target. Figures are normalized to the (a) global maximum value, and (b) local maximum value.

4.4 A Case Study: Imaging a Target with an Interferer

A case study is performed to examine the proposed antenna designs and compare their imaging performances in terms of mitigating the interferers distortion effects on the image. A plane wave representing a target inside the FOV at 10° is imaged with the presence of another plane wave representing an interferer outside the FOV at 40°. Then, the image of the desired target presented alone and its image with the presence of the interferer are compared. The ideal image in any case is expected to be exactly similar to that of the target when presented alone. However, the actual reconstructed images possess some distortion due to the interferers. The goal is to compare between these distortions resulting from using the different proposed antenna designs. Three different cases are presented, with different interferer's strengths.

In the first case, both the target and the interferer have the same magnitude. The reconstructed images using the 64-elements uniform linear array, shown in Fig

4.9, and the flat-top antenna with a SLL of 20dB, shown in Fig 4.10, are compared. The resulting image using the flat-top antenna is closer to the expected image of the target. However, the effect of the interferer is not very obvious in this case. So, the magnitude of the interferer is increased to the double in the second case. The enhancement in the quality of the image is more obvious when comparing Fig 4.11 for the linear array and in Fig 4.12 for the flat-top antenna. Moreover, the magnitude of the interferer is further increased to be eight times as the target's magnitude in the third case shown in Fig 4.13 and Fig 4.14. Again, this comparison explains clearly the enhancement achieved by using the flat-top antenna over the linear array.

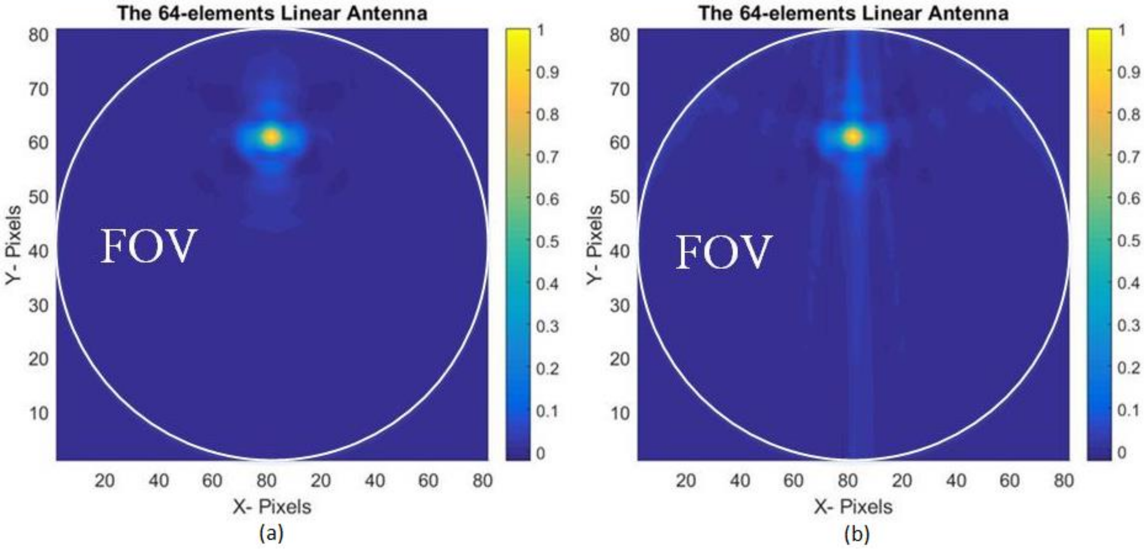

Figure 4-9 The reconstructed images using the linear array of a plane wave representing a target at 10° when it is (a) presented alone, and (b) with another plane wave represnting an interferer at 40° with the same magnitude as the target. Figures are normalized to the local maximum in each case.

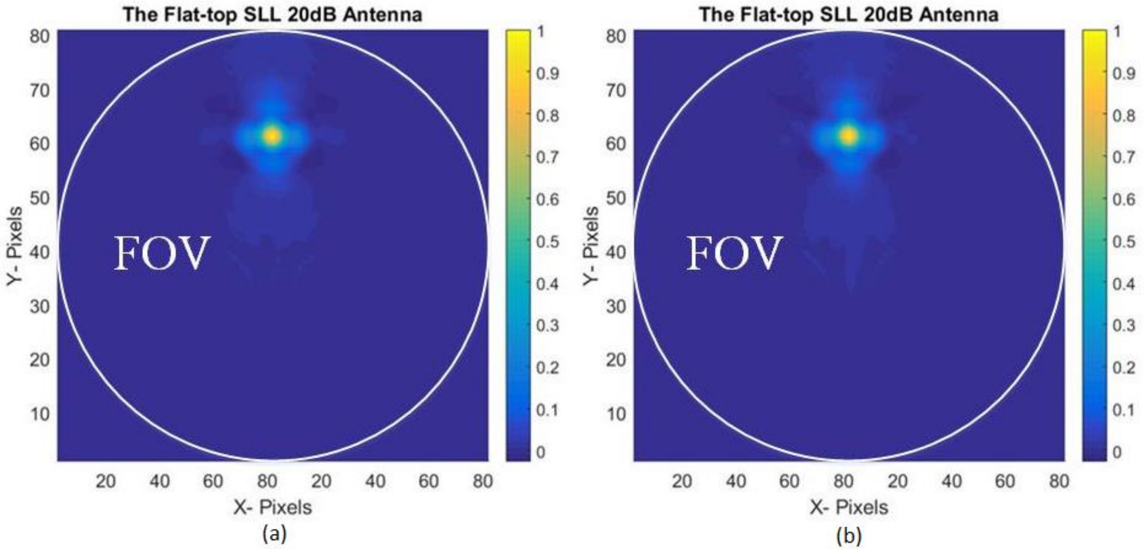

Figure 4-10 The reconstructed images using the flat-top antenna with SLL of 20dB of a plane wave representing a target at 10° when it is (a) presented alone, and (b) with another plane wave represnting an interferer at 40° with the same magnitude as the target. Figures are normalized to the local maximum in each case.

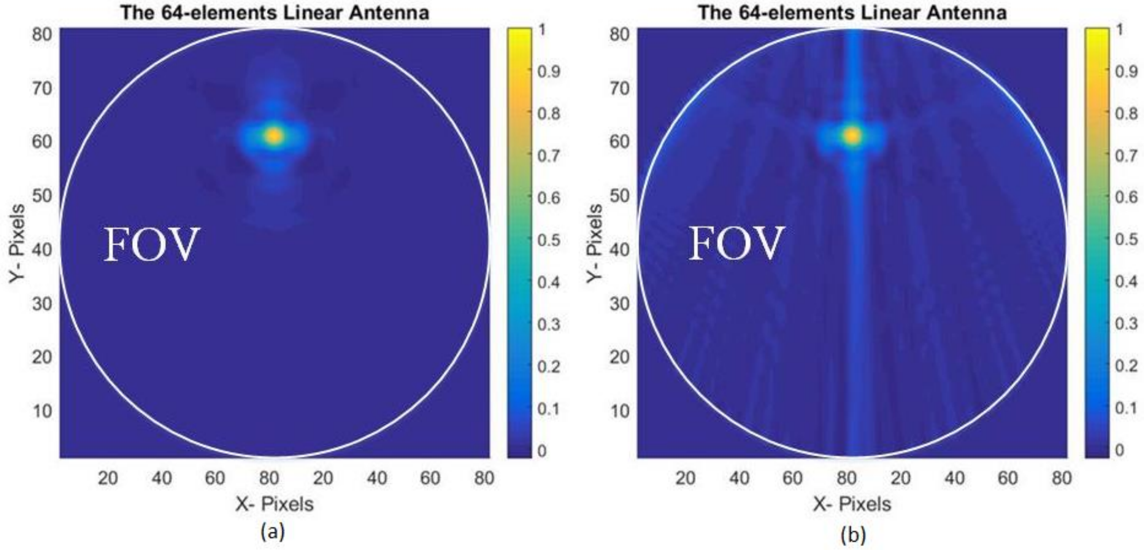

Figure 4-11 The reconstructed images using the linear array of a plane wave representing a target at 10° when it is (a) presented alone, and (b) with another plane wave represnting an interferer at 40° with double the magnitude of the target. Figures are normalized to the local maximum in each case.

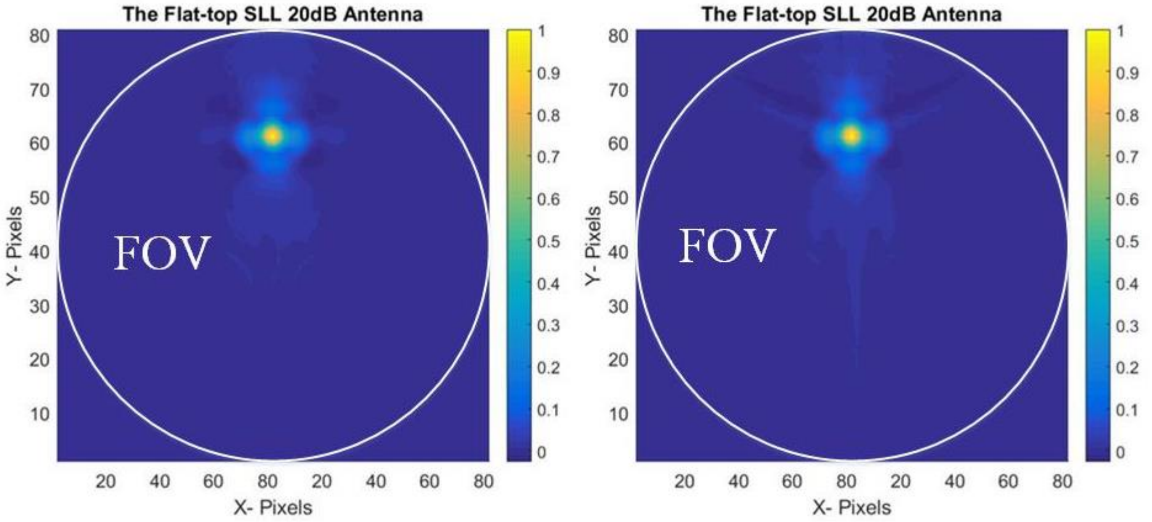

(a) (b)

Figure 4-12 The reconstructed images using the flat-top antenna with SLL of 20dB of a plane wave representing a target at 10° when it is (a) presented alone, and (b) with another plane wave represnting an interferer at 40° with double the magnitude of the target. Figures are normalized to the local maximum in each case.

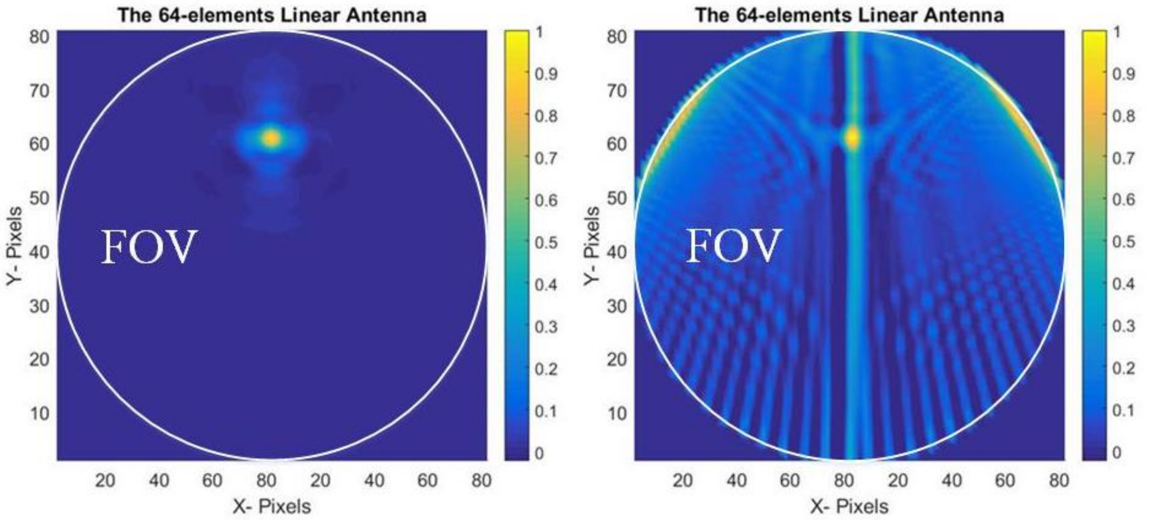

(a) (b)

Figure 4-13 The reconstructed images using the linear array of a plane wave representing a target at 10° when it is (a) presented alone, and (b) with another plane wave represnting an interferer at 40° with an eight times the magnitude of the target. Figures are normalized to the local maximum in each case.

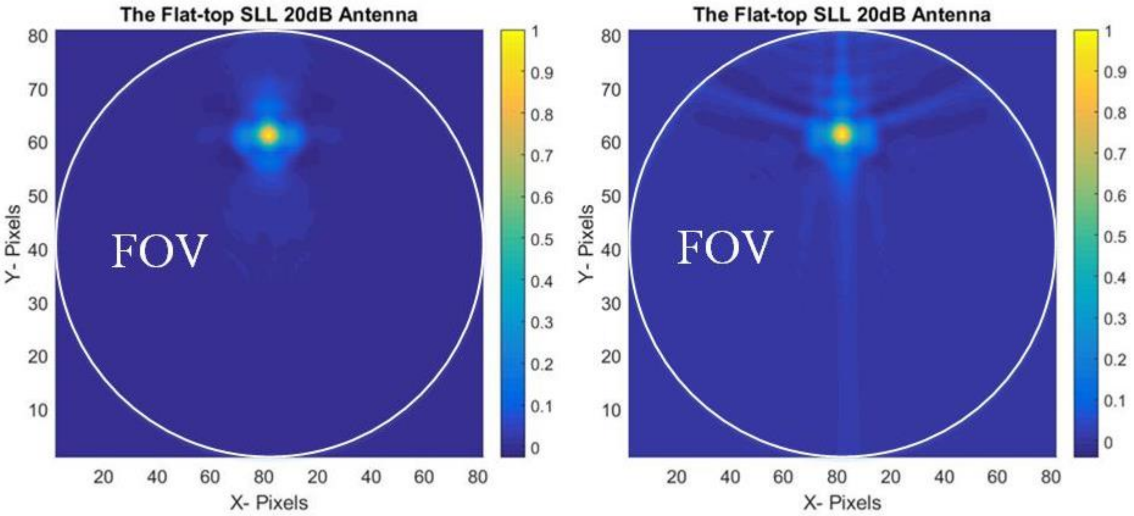

(a) (b)

Figure 4-14 The reconstructed images using the flat-top antenna with SLL of 20dB of a plane wave representing a target at 10° when it is (a) presented alone, and (b) with another plane wave represnting an interferer at 40° with an eight times the magnitude of the target. Figures are normalized to the local maximum in each case.

CHAPTER 5

CONCLUSIONS AND FUTURE WORK

5.1 Summary and Conclusions

In this thesis, two phased-array antenna designs for compact THz imaging systems are proposed and compared. These designs are taking advantage of the Fourier-slice theorem to reconstruct the image of the targets in the required FOV. This imaging algorithm allows for a significant reduction in the number of elements in the antenna array as it requires illuminating a linear portion of the FOV at a time instead of illuminating point by point. Therefore, much simpler RF front-ends will be required in the system to feed this antenna.

However, the implementation of the Fourier-slice theorem introduces the need to mechanically rotate the antenna to different projection angles to reconstruct the image. So, in comparison to a fully electronic sweeping algorithm, this technique increases the acquisition time because of the significant difference in speed between mechanical and electronic sweeping. However, it is still faster than the raster scanning technique for example which requires mechanical motion in two degrees of freedom to scan the FOV. While in our case the antenna needs to be mechanically rotated in only one degree of freedom. Also, using a mechanical rotor will increase the total weight and size of the system significantly. However, this imaging system can take advantage of platforms that have inherent rotating parts like drones.

Two proposed antenna designs that can implement the Fourier-slice theorem technique for 2D imaging are presented. The first design comprised a 64-element linear uniform array with a fan-beam radiation pattern. This design suffers from the wide beamwidth in the *H*-plane which extends beyond the required FOV allowing for any interferer outside the FOV to distort the image of the required target. This drawback was excluded in a novel flat-top 14×64 elements non-uniform antenna array that has a limited HPBW to focus its radiation within the desired FOV dimensions. This design allows to mitigate the interference effect from any object outside the desired FOV enhancing the quality of imaging. This enhancement was proven by comparing the simulation results of imaging a phantom object as a target at 300 GHz using both the uniform linear array and the flat-top array. However, this enhancement in the imaging quality comes at the cost of increasing the complexity of the system by increasing the number of elements in the array from 64 to 14×64 = 896.

Finally, a novel simulation algorithm is used to reduce the simulation time of the imaging process. This algorithm allows for computing the radiated fields of the antenna array at all the scanning angles and the scattering fields from the target only once. While, the fields are rotated in Matalb to account for the different projection angles. An enhancement in the simulation time equals to the number of the required projection angles, 90 times in our case, is achieved.

5.2 Current Challenges and Future Work

Despite the afore-mentioned improvements in the imaging system, several challenges are considered for future work:

- The possible fluctuations of the rotating platform might affect the quality of the reconstructed image, so they must be modeled and taken into account during the post-processing of the image.

- The curvature of the radiated fan beam from the antenna, especially at large tilting angles, revokes the assumption of performing a parallel beam projection and will affect the image. So, this curvature also needs to be modeled and considered in the post-processing to correct for its effects on the image.
- Investigating the impact of using the asymmetric excitation coefficients on the reconstructed images to simplify the required feeding network.
- The design of the feeding circuit for both designs while trying to keep it as simple as possible to decrease the size, weight, and cost of the system.
- More practical types of radiating elements need to be used for the system to be low profile and easy to fabricate. So, instead of using dipoles, patch antennas may be considered.
- The fabrication and measurements for a prototype of the system to compare results with those of the simulations.

REFERENCES

[1] M. Herzberger, "Optics from Euclid to Huygens," Appl. Opt.5, 1383-1393, 1966.

[2] JH. Scatliff and PJ. Morris, “From Roentgen to magnetic resonance imaging: the history of medical imaging,” N C Med J. 2014; 75:111–113.

[3] WG. Bradley, “History of Medical Imaging,” Proceedings of the American Philosophical Society. 152, 3, 349-361, Sept. 2008. ISSN: 0003049X.

[4] R. Lai *et al.*, "Sub 50 nm InP HEMT Device with Fmax Greater than 1 THz," *2007 IEEE International Electron Devices Meeting*, Washington, DC, 2007, pp. 609-611. doi: 10.1109/IEDM.2007.4419013.

[5] E. J. Nichols and J. D. Tear, “Joining the Infrared and Electric Wave Spectra”, Astrophys. J., vol.61, pp. 17-37, 1925.

[6] E. Bründermann, H. Hübers and M. F. Kimmitt. Terahertz Techniques. Springer, 2012. pp.301-340.

[7] B. B. Hu and M. C. Nuss, "Imaging with Terahertz Waves," Opt. Lett. 20, 1716-1718, 1995.

[8] A. G. Davies, E. H. Linfield and M. B. Johnston, “The Development of Terahertz Sources and their Applications,” Physics in Medicine and Biology, Oct 17, 2002.

[9] H. B. Liu, H. Zhong, N. Karpowicz, Y. Chen and X. C. Zhang, “Terahertz Spectroscopy and Imaging for Defense and Security Applications,” in Proceedings of the IEEE, vol. 95, no. 8, pp. 1514-1527, Aug. 2007.

[10] D. A. Wikner, “Progress in millimeter-wave imaging,” Proc. SPIE 7936, RF and Millimeter-Wave Photonics, Feb. 2011.

[11] R. W. McMillan, "Terahertz Imaging, Millimeter-Wave Radar," Advances in Sensing with Security Applications, 2, pp. 243 -268, Springer, Netherlands, 2006.

[12] K. B. Cooper, R. J. Dengler, N. Llombart, B. Thomas, G. Chattopadhyay and P. H. Siegel, "THz Imaging Radar for Standoff Personnel Screening," in IEEE Transactions on Terahertz Science and Technology, vol. 1, no. 1, pp. 169-182, Sept. 2011.

[13] D. M. Sheen, D. L. McMakin and T. E. Hall, "Three-dimensional millimeter-wave imaging for concealed weapon detection," in IEEE Transactions on Microwave Theory and Techniques, vol. 49, no. 9, pp. 1581-1592, Sep 2001.

[14] B. Gonzalez-Valdes, Y. Alvarez, S. Mantzavinos, C. M. Rappaport, F. Las-Heras and J. A. Martinez-Lorenzo, "Improving Security Screening: A Comparison of Multistatic Radar Configurations for Human Body Imaging," in IEEE Antennas and Propagation Magazine, vol. 58, no. 4, pp. 35-47, Aug. 2016.

[15] L. Pulido-Mancera, T. Fromenteze, T. Sleasman, M. Boyarsky, M. Imani, M. Reynolds, and D. Smith, "Application of range migration algorithms to imaging with a dynamic metasurface antenna," J. Opt. Soc. Am. B 33, 2082-2092 (2016).

[16] S. S. Ahmed, A. Schiessl and L. P. Schmidt, "A Novel Fully Electronic Active Real-Time Imager Based on a Planar Multistatic Sparse Array," in IEEE Transactions on Microwave Theory and Techniques, vol. 59, no. 12, pp. 3567-3576, Dec. 2011.

[17] B. Baccouche; P. Agostini; S. Mohammadzadeh; M. Kahl; C. Weisenstein; J. Jonuscheit; A. Keil; T. Loeffler; W. Sauer-Greff; R. Urbansky; P. Haring Bolivar; F. Friederich, "3D Terahertz Imaging with Sparse Multistatic Line Arrays," in IEEE Journal of Selected Topics in Quantum Electronics, vol.PP, no.99, pp.1-1

[18] S. Nowok, R. Herschel, R. Zimmermann, A. Shoykhetbrod, S. A. Lang and N. Pohl, "3D imaging system based on a MIMO approach at 360GHz for security screening," 2016 Progress in Electromagnetic Research Symposium (PIERS), Shanghai, 2016, pp. 671-675.

[19] G. C. Trichopoulos, H. L. Mosbacker, D. Burdette and K. Sertel, "A Broadband Focal Plane Array Camera for Real-time THz Imaging Applications," in IEEE Transactions on Antennas and Propagation, vol. 61, no. 4, pp. 1733-1740, April 2013.

[20] M. C. Kemp, P. F. Taday, B. E. Cole, J. A. Cluff, A. J. Fitzgerald, W. R. Tribe, “Security applications of terahertz technology”, Proc. SPIE 5070, Terahertz for Military and Security Applications, 44, Aug 2003.

[21] A. J. Fitzgerald, E. Berry, N. N. Zinovev, G. C. Walker, M. A. Smith, J. M. Chamberlain, “An introduction to medical imaging with coherent terahertz frequency radiation”, in Physics in Medicine and Biology, Vol 47, No. 7, March 2002.

[22] T. D. Dorney, R. G. Baraniuk, D. M. Mittleman, “Material parameter estimation with terahertz time-domain spectroscopy”, in J. Opt. Soc. Am. A/Vol. 18, No. 7/July 2001.

[23] E. G. Yakovlev et al., “Nondestructive Testing of Polymer Composite Materials using THz Radiation,” in Journal of Physics, Conference Series 486 (2014).

[24] De Maagt, P., Bolivar, P. H. and Mann, C. 2005. Terahertz Science, Engineering and Systems—from Space to Earth Applications. Encyclopedia of RF and Microwave Engineering.

[25] B. Ma et al., “Spitzer Imaging of Strongly Lensed Hershel-Selected Dusty Star-Forming Galaxies,” in The Astrophysical Journal. 814:17 (13pp), Nov 2015.

[26] E. P. Kropotkina, S. V. Solomonov, S. B. Rozanov, A. N. Ignatyev, A. N. Lukin, "Ground-based millimeter-wave ozone monitoring in Moscow during sudden stratospheric warmings", Physics and Engineering of Microwaves Millimeter and Submillimeter Waves (MSMW) 2016 9th International Kharkiv Symposium on, pp. 1-3, 2016.

[27] N. Bajwa, J. Au, R. Jarrahy, S. Sung, M. C. Fishbein, D. Riopelle, D. B. Ennis, T. Aghaloo, M. A. St. John, W. S. Grundfest, and Z. D. Taylor, "Non-invasive terahertz imaging of tissue water content for flap viability assessment," Biomed. Opt. Express 8, 460-474 (2017).

[28] D. Banerjee, W. von Spiegel, M. D. Thomson, S. Schabel, and H. G. Roskos, "Diagnosing water content in paper by terahertz radiation," Opt. Express 16, 9060-9066 (2008).

[29] Gente, Ralf, and M. Koch. “Monitoring Leaf Water Content with THz and Sub-THz Waves.” Plant Methods 11 (2015).

[30] Ergün, S., Sönmez, S. (2015). Terahertz Technology for Military Applications, Journal of Military and Information Science, Vol3(1),13-16.

[31] Iwaszczuk, K., Jepsen, P. U., & Heiselberg, H. (2012). Terahertz Technology for Defense and Security-Related Applications. Kgs. Lyngby: Technical University of Denmark (DTU).

[32] H. T. Chen, R. Kersting, and G. C. Cho, “Terahertz Imaging with nanometer resolution,” in Applied Physics Letters, Vol 83, No 15., Oct 2003.

[33] K. Wu, Y. J. Cheng, T. Djerafi and W. Hong, "Substrate-Integrated Millimeter-Wave and Terahertz Antenna Technology," in Proceedings of the IEEE, vol. 100, no. 7, pp. 2219-2232, July 2012.

[34] H. Wang, "Review of CMOS millimeter-wave radio frequency integrated circuits," 2015 IEEE MTT-S International Microwave and RF Conference (IMaRC), Hyderabad, 2015, pp. 239-242.

[35] A. Tang, T. Reck and G. Chattopadhyay, "CMOS system-on-chip techniques in millimeter-wave/THz instruments and communications for planetary exploration," in IEEE Communications Magazine, vol. 54, no. 10, pp. 176-182, October 2016.

[36] G. R. Lockwood and F. S. Foster, "Optimizing sparse two-dimensional transducer arrays using an effective aperture approach," 1994 Proceedings of IEEE Ultrasonics Symposium, Cannes, France, 1994, pp. 1497-1501 vol.3.

[37] C. A. Wiley, “Fanbeam inversion radar,” US 4 739 332 A, April 19, 1988.

[38] A. C. Kak and M. Slaney, “Principles of Computerized Tomographic Imaging,” IEEE Press, 1988.

[39] Ergün, S., Sönmez, S. (2015). Terahertz Technology for Military Applications, Journal of Military and Information Science, Vol3(1),13-16.

[40] D. C. Munson, J. D. O'Brien and W. K. Jenkins, "A Tomographic Formulation of Spotlight-mode Synthetic Aperture Radar," in Proceedings of the IEEE, vol. 71, no. 8, pp. 917-925, Aug. 1983.

[41] P. C. Theofanopoulos and G. C. Trichopoulos, "A novel THz radar imaging system using the radon transform," 2017 IEEE International Symposium on Antennas and Propagation & USNC/URSI National Radio Science Meeting, San Diego, CA, 2017, pp. 1513-1514.

[42] Radon, Johann (1917), "Über die Bestimmung von Funktionen durch ihre Integralwerte längs gewisser Mannigfaltigkeiten", Berichte über die Verhandlungen der Königlich-Sächsischen Akademie der Wissenschaften zu Leipzig, Mathematisch-Physische Klasse [Reports on the proceedings of the Royal Saxonian Academy of Sciences at Leipzig, mathematical and physical section], Leipzig: Teubner (69): 262–277; Translation: Radon, J.; Parks, P.C. (translator) (1986), "On the determination of functions from their integral values along certain manifolds", IEEE Transactions on Medical Imaging, 5 (4).

[43] C. A. Balanis, *Antenna Theory: Analysis and Design*. John Wiley & Sons, 2016.

[44] S. A. Schelkunoff, "A Mathematical Theory of Linear Arrays," Bell System Technical Journal, Vol 22, pp. 80-107, 1943.

[45] R. S. Elliott, "Improved Pattern Synthesis for Equispaced Linear Arrays," Alta Frequenza, Dec 1982.

[46] C. L. Dolph, "A Current Distribution for Broadside Arrays Which Optimizes the Relationship between Beamwidth and Side Lobe Level," Proc. IRE, 34 (1946), 335-48.

[47] T. T. Taylor, "Design of Line Source Antennas for Narrow Beamwidth and Low Side Lobes," IRE Trans. Antennas and Propagation, AP-7 (1955), 16-28.

[48] E. T. Bayliss, "Design of Monopulse Antenna Difference Patterns with Low Side Lobes," Bell System Tech. J., 47 (1968), 623-40.

[49] R. S. Elliott, G. J. Stern, "A New Technique for Shaped Beam Synthesis of Equispaced Arrays," IEEE Transactions on Antennas and Propagation, vol. AP-32, no. 10, October 1984.

[50] H. J. Orchard, R. S. Elliott and G. J. Stern, "Optimising the Synthesis of Shaped Beam Antenna Patterns," IEE Proceedings, vol. 132, Pt. H, no.1, Feb 1985.

[51] P. C. Theofanopoulos and G. C. Trichopoulos, "Modeling of mmW and THz Imaging Systems Using Conjugate Field Coupling," in *IEEE Antennas and Wireless Propagation Letters*, vol. 17, no. 2, pp. 213-216, Feb. 2018.

[52] FEKO 14.1 Stellenbosch, South Africa, E. S. Systems. Available: http://www.feko.info